

Optical Properties and Applications of Plasmonic-Metal Nanoparticles

Lu Wang, Morteza Hasanzadeh Kafshgari, and Michel Meunier*

Noble metal nanoparticles due to their unique optical properties arising from their interactions with an incident light have been intensively employed in a broad range of applications. This review comprehensively describes fundamentals behind plasmonics, used to develop applications in the fields of biomedical, energy, and information technologies. Basic concepts (electromagnetic interaction and permittivity of metals) are discussed through Mie theory presented as the main model for interpreting phenomena of optical absorption and scattering. The effects of near-field enhancement, shape, composition, and surrounding medium of nanoparticles on optical properties are described in detail. The review explores and identifies the potential of plasmonic nanoparticles based on their optical properties (e.g., light absorption, scattering, and field enhancement) for developing different applications (biomedical, energy and information technologies). Due to a significant impact of plasmonic nanoparticles on medicine and healthcare products and technologies, the review initially focuses on biomedical applications extensively benefited from optical features of these nanoparticles. Advantages of the optical properties outstandingly implemented are also briefly discussed in other applications, including energy and information technologies. This review concisely summarizes the explored areas based on plasmonic properties, compares advantages of plasmonic nanoparticles over other types of nanomaterials and highlights challenges.

1. Introduction

Metallic nanoparticles (NPs) are among the most popular nanomaterials, stimulated by an incident light, to spark a wide range of applications to well-established performances.^[1] Noble metal NPs exhibit a number of properties that make them attractive for a wide range of applications in biomedical, energy, and information technologies. Due to the interaction of these metallic nanostructures with an incident light, a collective oscillation of free electrons, called plasmon, becomes dominant and generates the surface plasmon resonance. A large number of these electrons, participating in the surface plasmon resonance, causes a strong absorption and scattering, as well as the near-field enhancement at the natural frequency of plas-

monic-metal nanoparticles.^[2] The localized surface plasmon resonance (LSPR) phenomena acquired by noble metal NPs are well known due to their resonance frequency in both visible and near-infrared ranges and studied to develop biomedical, energy, and information technologies (e.g., bioimaging, biosensing, nanosurgery, photocatalysis, and data storage).^[1a,3] To achieve an adaptable and application-oriented LSPR peak, physical features, including size, morphology, and composition of noble metal NPs, need to be precisely designed by considering the permittivity of the surrounding medium.


Understanding physics behind the LSPR phenomena also plays a critical role in the fabrication and implementation of plasmonic NPs for developing various applications, and therefore many calculation approaches (e.g., Mie theory and numerical simulations) have been proposed to describe the LSPR phenomena of metallic NPs. Metallic NPs such as Ag, Au, and Pt with their tunable LSPR can easily be combined with other materials (e.g., titanium, silicon, carbon, and

a wide range of polymers) for synergizing specific applications.^[4] Synthesis of almost all metallic NPs is environmentally friendly compared to other nanomaterials (e.g., carbon-based materials), requiring harsh chemical agents for the reduction and oxidation.

Compared to other nanomaterials, plasmonic properties of noble metal NPs stand out from most other nanomaterials. The optical properties, including enormous absorption, scattering, and field enhancement, enable a wide range of applications associated with opto-signal or enhanced chemical signals for imaging and sensing. Moreover, their reproducible fabrication protocols and tunable optical properties are outstanding due to an adaptable relation between plasmonic structures and optical properties.^[5] The irreplaceable and valuable optical properties of noble metals can be evaluated by precise plasmonic theories, assisting a reproducible fabrication of application-oriented plasmonic nanomaterials, followed by their feasible surface modification tackling problems related to functionality in complex environments compared to other nanomaterials.^[6]

In this review, we summarize fundamental aspects of the surface plasmonics employed to design elaborated nanoparticles and implement their application-oriented plasmonic properties (Figure 1). A comprehensive description and comparison of

L. Wang, Dr. M. Hasanzadeh Kafshgari, Prof. M. Meunier
Department of Engineering Physics
Polytechnique Montréal
Montreal, QC H3C 3A7, Canada
E-mail: michel.meunier@polymtl.ca

 The ORCID identification number(s) for the author(s) of this article can be found under <https://doi.org/10.1002/adfm.202005400>.

DOI: 10.1002/adfm.202005400

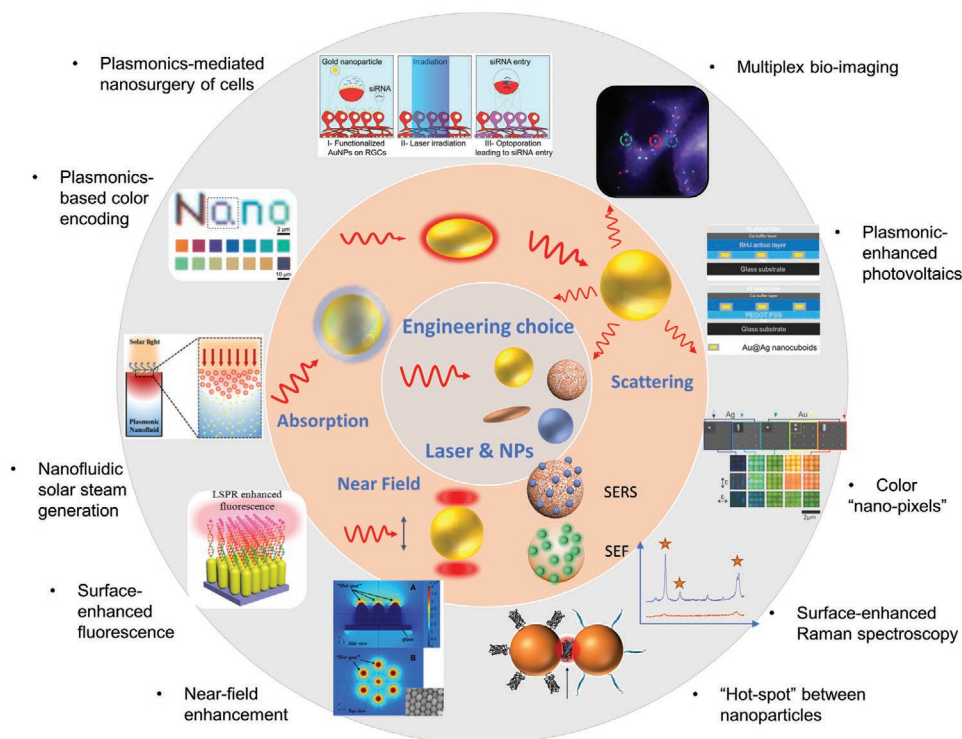


Figure 1. Schematic representation from plasmonic nanostructure design to applications. The center circle shows the engineering choice of the plasmonic nanostructures (geometry and composition) and irradiation light (wavelength, pulse width, energy, etc.). The second inner circle represents the main phenomena namely absorption, scattering, and near field. The outside circle shows examples of various applications exploiting specific phenomena, based on the engineering choices. Reproduced with permission.^[7a] Copyright 2018, American Chemical Society. Reproduced with permission.^[7b] Copyright 2019, John Wiley & Sons, Inc. Reproduced with permission.^[7c] Copyright 2016, Royal Society of Chemistry. Reproduced with permission.^[7d] Copyright 2016, John Wiley & Sons, Inc. Reproduced with permission.^[7e] Copyright 2018, Springer Nature Limited. Reproduced with permission.^[7f] Copyright 2017, American Chemical Society. Reproduced with permission.^[7g] Copyright 2017, Elsevier B.V. Reproduced with permission.^[7h] Copyright 2016, American Chemical Society.

different optical properties related to the electromagnetic interaction, composition, shape, and permittivity of plasmonic nanoparticles as well as the surrounding medium are given. The fundamentals of scattering and extinction cross sections based on “Mie theory” are also presented to interpret a broad range of application-oriented plasmonic spherical nanoparticles. Applications of plasmonic-metal nanoparticles in three important fields (biomedical, energy, and information technology) based on the light absorption, scattering, and field enhancement are summarized and discussed. Owing to their remarkable properties, such as optical responses, surface reactivity, and long-term physico-chemical stability *in vitro* and *in vivo*, we extensively focus on biomedical applications of novel approaches, which can eventually be translated into clinical settings. We then continue discussing the use of plasmonic properties in developing energy technologies by taking advantage of their large scattering cross section, field enhancement at the surface, and carrier generation in the substrate. Major potential of plasmonic NPs is examined in energy technologies (e.g., photovoltaic energy conversion and photocatalysis), and their unsolved challenges are highlighted. In the final part, our attention is focused on current achievements of plasmonic nanoparticles in information technology. We briefly discuss important roles of plasmonic nanoparticles for furthering data storage and encryption, and outline limitations and challenges that need to be addressed in order to accelerate their practical outcomes in information technology.

2. Plasmonic Nanomaterials

As explained in the introduction, LSPR phenomenon is the intrinsic characteristic of plasmonic materials. Besides noble metals mostly developed for a wide range of applications, there exist other types of plasmonic nanomaterials.^[8] LSPR has also been discovered in other materials, including heavily doped semiconductors, metal oxides, 2D materials, conducting polymers, summarized in **Table 1**. These materials have their intrinsic resonance wavelength range, tunable by adjusting morphology and size in order to cover a broad-spectrum range. Depending on the purpose of an application as well as cost effectiveness, these materials offer a wide range of choices that can be designed in combination with other different materials.^[8a,e,f,h] In general, semiconductors have resonance redshifted compared to the visible and near-infrared (NIR) range of most metallic materials, and small size (<10 nm) of semiconductor particles, like quantum dots, can be applied in biomedical applications. However, metallic NPs, especially Ag, have the highest resonance intensity, facilitating the on-resonance applications. Each kind of nanomaterials has their advantages and disadvantages, and specific material suitable for all applications has not been found. Nowadays, metallic plasmonic NPs have the dominant position in plasmonics, in terms of theoretical study and practical applications. These metallic NPs show significant advantages due to their large scattering

Table 1. Properties of different plasmonic materials.

Materials	Mechanism	Examples	LSPR range	Advantages	Comments
Metallic nanostructures	Free electrons	Au, Ag, Cu and their alloys	UV–visible	Mature theory of optical properties, various structures, controllable synthesis methods, strong plasmonic effects	Costly, limited permittivity
Semiconductor nanocrystals	Free holes	Cu _{2-x} S, ^[9] Cu _{2-x} Se, ^[10] ITO, ^[11] TiN ^[12]	Visible-NIR	smaller size (<10 nm), broader NIR absorbance	Difficult to dope
2D materials	Electrons and holes	Graphene, ^[13] MoS ₂ ^[14]	NIR	strong plasmonic effect	Tedious synthesis processing, high-demanding synthesis instrument
Conductive polymers	Polaronic charge carriers	poly(3,4-ethylenedioxythiophene:sulfate) ^[15]	NIR	Switchable state, low cost, flexibility, biocompatibility	Limited to fundamental study, low electrical conductivity, high defect density

and absorption cross section, strong field enhancement, as well as easy formation of different reproducible morphologies. Therefore, our review focuses on metallic plasmonic nanostructures and summarizes valuable details for the understanding plasmonic properties, which may accelerate the utilization of other nonmetallic plasmonic materials.

3. Optical Properties of Plasmonic Nanoparticles

3.1. Electromagnetic Interaction with Plasmonic Nanoparticles

Upon incidence of an electromagnetic wave, free electrons of metallic NPs are driven to the surface opposite to the direction of the electric field, resulting in positively and negatively charged sides for each particle. The electron distribution counteracts the incident electric field inside the particle and only enhances the field at its surface to generate well-performance conductors.^[1a] At a specific wavelength, LSPR peak, the charge-induced field, results in an induced dipole that may be considered to be spatially invariant within NPs with diameter smaller than ≈20 nm, but varying with time, following the electric field of the incident electromagnetic wave. For larger NPs, higher orders poles or multipoles must be considered to describe the charge-induced field.

The collective oscillation of the electrons yields a large optical extinction cross section (σ_e) of NPs, including the contributions of both scattering and absorption. As a consequence of the interaction with a light, the induced dipole oscillator emits the light at the same frequency as the incident light, being scattered in all directions. The effective area of the particle, scattering the light, is defined as the scattering cross section (σ_{scat}).^[16] In addition, the electric resistance of NPs is responsible for absorption of the incident light, since the metallic NPs are not perfect conductors, and therefore the oscillating electrons lose some of their energy in the form of heat. The corresponding effective area of absorbing light is the absorption cross section (σ_{abs}). The absorption feature can efficiently be used for a localized heating application, for example, hyperthermia in cancer therapy.^[17] In short, the extinction cross section is defined as

$$\sigma_{\text{ext}} = \sigma_{\text{scat}} + \sigma_{\text{abs}} \quad (1)$$

It corresponds to the total lost (by scattering and absorption) when the light is incident on NPs. The optical cross sections

are dependent upon the induced dipole, controlled by multiple factors (e.g., composition, size, and shape of NPs, the surrounding medium, and the wavelength of the incident electromagnetic wave). Certainly, plasmonics is of great importance because the scattering, absorption and extinction cross sections can become tremendous when the incident light reaches the resonance condition.^[17a,18] The phenomenon results in one or more peaks in the scattering, absorption or extinction spectra, known as plasmonic resonance peaks.

3.2. Permittivity of Metals

The optical properties of metal NPs primarily depend upon the permittivity, $\epsilon(\omega)$, which is composed of both real ($\epsilon_r(\omega)$) and imaginary parts ($\epsilon_i(\omega)$)

$$\epsilon(\omega) = \epsilon_r(\omega) + i\epsilon_i(\omega) \quad (2)$$

where ω is the radial frequency. In general, the position of resonance peak is mostly determined by the real part, while the dephasing depends on the imaginary part.^[1a]

Figure 2a,b shows the experimental real and imaginary parts of Ag, Au, Al, and Cu.^[19] The behavior of these curves can be described by many contributions, including the ones from free electrons and interband transitions. The simplest model to describe the permittivity of metal is the Drude model in which conduction electrons are considered to be free electrons.^[21] Therefore, it can be expressed as

$$\epsilon(\omega) = 1 - \frac{\omega_p^2}{\omega(\omega + i\gamma_b)} \quad (3)$$

where ω_p is the plasma frequency and γ_b is the bulk damping constant related to the Fermi velocity v_F and the mean free path l_m , as

$$\gamma_b = \frac{v_F}{l_m} \quad (4)$$

The Fermi velocity is calculated by using the electron density, vacuum permittivity and effective mass of the electrons. It varies with the electron density of different metals. The mean free path depends upon the effects of various factors, such as phonons and impurities. For example, v_F and γ_b for Au are

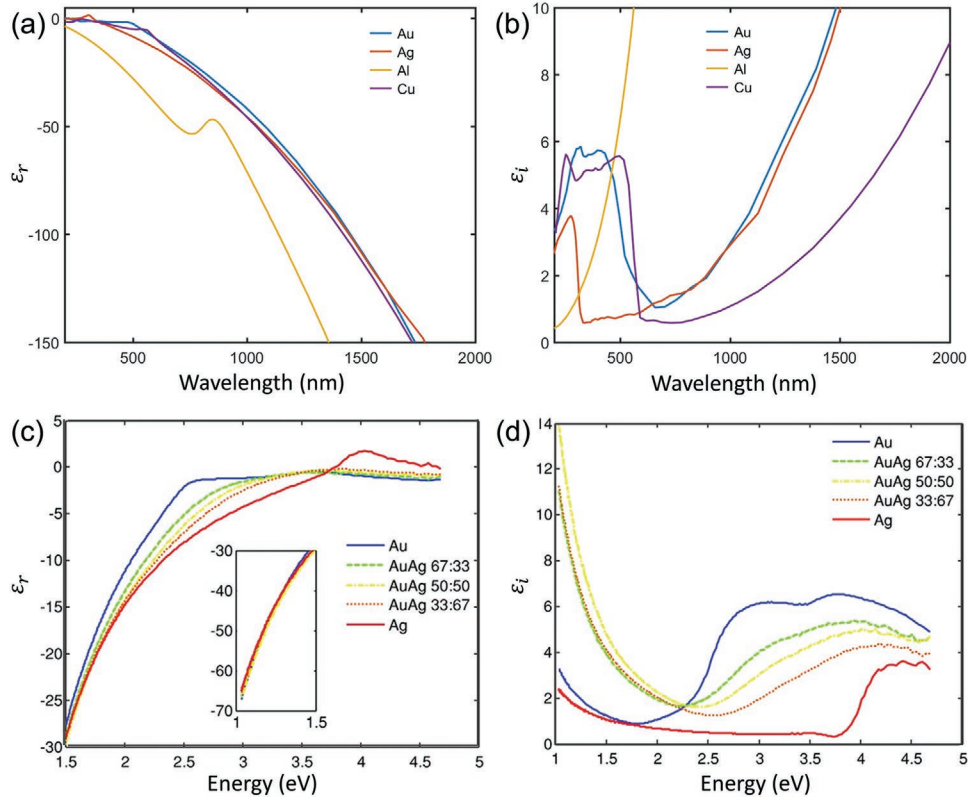


Figure 2. a) Real and b) imaginary parts of permittivity as a function of wavelength for Au, Ag, Al, and Cu as obtained experimentally. c) Real and d) imaginary part of dielectric constants of Au, Ag, and Au/Ag alloy thin films as a function of energy. Reproduced with permission.^[20] Copyright 2013, John Wiley & Sons, Inc.

$v_F = 1.4 \times 10^6 \text{ ms}^{-1}$ and $\gamma_b = (15 \text{ fs})^{-1}$, resulting in a mean free path of $l_m = 21 \text{ nm}$ at room temperature.^[1a,21] When the diameter of NPs is smaller than the l_m , the surface effect should be taken into consideration.

$$\gamma(l_{\text{eff}}) = \gamma_b + \frac{A v_F}{l_{\text{eff}}} \quad (5)$$

where l_{eff} is the effective path length, which is the average distance the electrons travel before scattering off a surface, and A is a dimensionless constant representing the electron-surface interaction.^[1a] The value of l_{eff} is related to the shape of NPs, and can be calculated by volume V and surface S of the NP, as $l_{\text{eff}} = 4V/S$.^[22]

Interband transitions are obtained from the lower-energy electrons compared to free electrons, and their effect only becomes large when the incident energy is high enough. Some interband transition energies, for example, are 3.9 eV for Ag, 2.4 eV for Au, and 2.1 eV for Cu. The interband transition will affect the frequency dependence of damping and can be taken into account by adding a term to the permittivity

$$\varepsilon(\omega) = \varepsilon^{\text{ib}}(\omega) + 1 - \frac{\omega_p^2}{\omega(\omega + i\gamma(l_{\text{eff}}))} \quad (6)$$

This term can be separated into real and imaginary parts, as $\omega \gg \gamma$

$$\varepsilon_r(\omega) \approx \varepsilon_r^{\text{ib}}(\omega) + 1 - \frac{\omega_p^2}{\omega^2} \quad (7)$$

and

$$\varepsilon_i(\omega) \approx \varepsilon_i^{\text{ib}}(\omega) + \frac{\omega_p^2 \gamma(l_{\text{eff}})}{\omega^3} \quad (8)$$

Since l_{eff} does not appear in the real part for small NPs, it is almost the same as for bulk: $\varepsilon_r(\omega) \approx \varepsilon_r^{\text{b}}(\omega)$. The imaginary part depends strongly on $\gamma(l_{\text{eff}})$, indicating that the most significant size factor influences the damping with an electron surface scattering.

The condition for considering surface scattering of electrons depends on the dimension of NPs that should be smaller than the mean free path, l_m . Due to the quantum confinement, very small particles are no longer conductors, and therefore the Drude model is no longer the appropriate description.

In addition to pure metals, their alloys can also play a significant role in terms of permittivity.^[23] Au/Ag alloy permittivity, for example, has recently been determined. The real and imaginary parts measured by ellipsometry for several compositions are shown in Figure 2c,d. Interband transitions shift progressively from Au ($\approx 2.5 \text{ eV}$) to Ag ($\approx 4 \text{ eV}$) and result in a similar shape for the real part, unlike the imaginary part. The alloys exhibit higher absorption than pure metals at the low energy.^[20]

Meunier and co-workers developed an analytical model for the prediction of the dielectric functions of Au/Ag alloys.^[20] These multi-parametric equations are based on the modification of the Drude–Lorentz model, considering the band structure of the different Au and Ag metals.

3.3. Scattering and Absorption of Spherical Nanoparticles

Gustav Mie was the first, in the early 1900s, who calculated the optical cross sections, σ_{sca} and σ_{ext} , of spherical NPs.^[24] Mie theory is a precise calculation based on Maxwell's equations for spherical particles, using the permittivity of NPs and their surroundings. The general expression for scattering and extinction cross sections are:

$$\sigma_{\text{sca}} = \frac{2\pi}{|\vec{k}|^2} \sum_{l=1}^{\infty} (2l+1) (|a_l|^2 + |b_l|^2) \quad (9)$$

$$\sigma_{\text{ext}} = \frac{2\pi}{|\vec{k}|^2} \sum_{l=1}^{\infty} (2l+1) (a_l + b_l) \quad (10)$$

where

$$a_l = \frac{\varepsilon_m m^2 j_l(x) [x j_l(x)]' - \varepsilon j_l(x) [m x j_l(mx)]'}{\varepsilon_m m^2 j_l(mx) [x h_l^{(1)}(x)]' - \varepsilon h_l^{(1)}(x) [m x j_l(mx)]'} \quad (11)$$

$$b_l = \frac{\varepsilon j_l(x) [x j_l(x)]' - \varepsilon_m j_l(x) [m x j_l(mx)]'}{\varepsilon j_l(mx) [x h_l^{(1)}(x)]' - \varepsilon_m h_l^{(1)}(x) [m x j_l(mx)]'} \quad (12)$$

j_l and h_l are respectively Bessel and Hankel functions. $x = |\vec{k}|R$, \vec{k} is the wave vector, and R is the geometric radius of NP; ε_m is the permittivity of the medium, and ε is the permittivity of the NP and $m = n/n_m$, where n is the complex refractive index of NP and n_m is that of surrounding medium. The number “ l ” corresponds to dipole ($l = 1$), quadrupole ($l = 2$), octupole ($l = 3$), and so on. Dipole theory can give cross sections when the size of spherical NPs is small compared to the wavelength of the incident light, typically when $R < \lambda/20$. The absorption and scattering cross section can be calculated in the dipolar approximation

$$\sigma_{\text{abs}} = \frac{24\pi^2 R^3 \varepsilon_m^{\frac{3}{2}}}{\lambda} \frac{\varepsilon_i}{|\varepsilon + 2\varepsilon_m|^2} \quad (13)$$

$$\sigma_{\text{scat}} = \frac{32\pi^4 R^6 \varepsilon_m^2}{\lambda^4} \left| \frac{\varepsilon - \varepsilon_m}{\varepsilon + 2\varepsilon_m} \right|^2 \quad (14)$$

where the permittivity of NPs, ε , is composed of real and imaginary parts, as $\varepsilon = \varepsilon_r + i\varepsilon_i$, and ε_m is the permittivity of the surrounding medium. According to these equations, for ε_i close to zero, the resonance condition occurs when $\varepsilon_r = -2\varepsilon_m$, resulting in extremely large σ_{ext} .^[25] The two requirements are satisfied only by a few metals, such as Au, Ag, and Cu. For very small NPs, $R \ll \lambda$, the extinction is essentially the absorption, $\sigma_{\text{ext}} \approx \sigma_{\text{abs}}$, as the scattering is negligible ($\sigma_{\text{scat}}/\sigma_{\text{abs}} \propto (R/\lambda)^3$). In

the dipole approximation, the internal field is considered to be proportional to the incident field, with a frequency-dependent factor, the local field factor, f

$$f(\omega) = \frac{3\varepsilon_m}{\varepsilon + 2\varepsilon_m} \quad (15)$$

This factor indicates that there may be an important field enhancement inside and around the particle as the different permittivities of particle and the media vary with the irradiating wavelength. This also indicates that the resonance condition is $\varepsilon_r = -2\varepsilon_m$.

In the dipole approximation, the plasmon peak occurs at $\frac{\omega_p}{\sqrt{1+2\varepsilon_m}}$. When the NPs become larger, $R > \lambda/20$, the internal field in the NPs cannot be assumed to be uniformly distributed into the NPs and, multipoles must be considered. The plasmon peak for the corresponding “ l ” can be approximated by

$$\omega_l = \frac{\omega_p}{\sqrt{1 + \frac{l+1}{l} \varepsilon_m}} \quad (16)$$

Only noble metals (e.g., Ag, Au, and Cu) have their LSPR in the range of ultraviolet (UV)–visible and NIR, while most other metals have resonance frequencies in the deep UV range, or higher frequencies.^[5b,25] Based on Mie theory, Meunier and co-workers have developed the NFMie program in order to theoretically calculate the optical cross section and field enhancement of arbitrary spherical NPs.^[20,26] For example, plasmon peaks, σ_{abs} , and σ_{scat} vary with diameter and composition of Au and Ag NPs (Figure 3a-i,b-i).

3.4. Surface Enhanced Effects

The plasmonic resonance leads to way larger optical cross sections when compared to the real dimensions of NPs, resulted from the amplification of the electromagnetic field around the NPs. Indeed, upon the irradiation by the incident light, the oscillation of free electrons generates an additional electric field near the surface of NPs, and enhances the original field if the phase delay is relatively small. For example, Figure 3a-ii,b-ii shows the electric field distribution of Au and Ag nanosphere (40–100 nm in diameter) at resonance frequency with a field amplification E/E_0 reaching close to ≈ 7 for Au and ≈ 14 for Ag.^[26]

When some molecules are in the near-field amplification of NPs, their fluorescence or Raman spectra can dramatically be enhanced. These phenomena lead to a greater surface enhanced Raman scattering (SERS) and surface enhanced fluorescence (SEF). This field enhancement effect is related to the intrinsic properties of plasmonic NPs and the incident light. In case of SEF-based applications, the molecule must not be too close in order to avoid quenching of the signal by the nearby presence of the metallic NP. However, this limitation is relatively minor for SERS-based applications, and the enhancement of the Raman signal near the surface of the NP can reach many orders magnitudes. Both the absorption of incident light

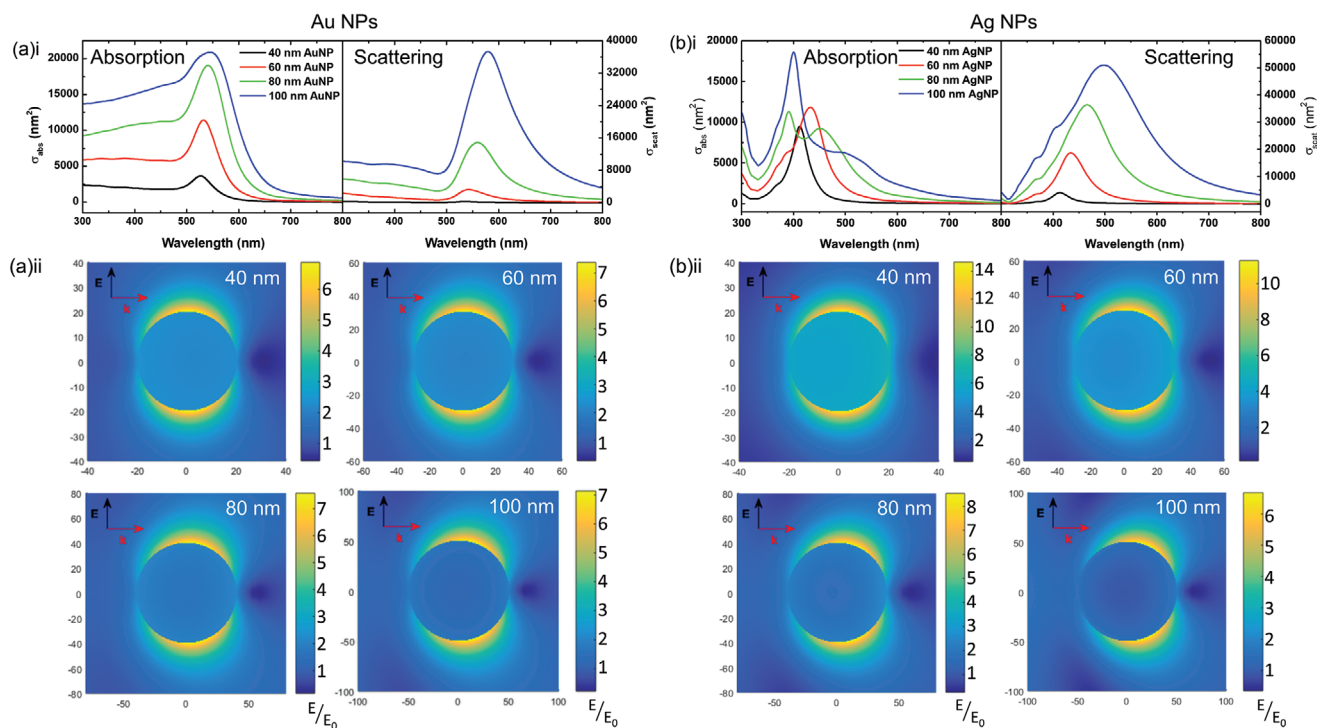


Figure 3. Absorption and scattering cross sections, σ_{abs} and σ_{scat} , of a-i) AuNPs and b-i) AgNPs in water with diameter of 40, 60, 80, and 100 nm, and (a-ii,b-ii) show their electric field enhancement (E/E_0) at the wavelength of scattering resonance, respectively. Calculations done by using Rioux and Meunier's developed NFMie program.^[26b]

and Raman signal depend on the local enhanced field. The enhancement factor G is given by

$$G = |E_{\text{local}}(\omega_L, r)|^2 |E_{\text{local}}(\omega_R, r)|^2 \quad (17)$$

where ω_L is the frequency of the incident light and ω_R is that of the Raman signal. As the Raman signal shift is very small, it may possible to assume that $\omega_L \approx \omega_R$, thus

$$G = |E_{\text{local}}(\omega_R, r)|^4 \quad (18)$$

For spherical nanoparticles, as the field enhancement may be near 10, G may be 10^4 – 10^6 . The enhancement also depends on the shape of the metallic nanostructures, especially narrow gap and high curvature of the surface.^[27] In general, sharp angles may lead to far bigger field enhancement of 100 to even 1000, resulting in G with an approximate value from 10^8 to 10^{12} , which have been implemented for a wide range of applications.^[28]

3.5. Shape Effects

Mie theory has been extended to other types of spheroidal NPs, including core–shell geometry with different metals or dielectric components.^[29] Considering a size-dependent electron surface scattering features of the shell, the effective free path can be modified in order to bring the scattering on the surface between core and shell into play. As confirmed by Mie theory, NPs composed of both metallic core or shell show significant

resonance shifts in a size-dependent manner. Encina and Coronado have applied Mie theory for simulating the extinction spectra of iron oxide@noble metal core–shell nanostructures. In their study, α - Fe_2O_3 @Ag core–shell NPs, for example, have been designed for obtaining an adaptable resonance peak and photothermal effect shift by varying the dimension of the core or the shell. **Figure 4** illustrates a dimension dependent heating effect under different irradiant wavelengths for α - Fe_2O_3 @Ag core–shell NPs.^[29b] Mie theory has been found beneficial for the prediction of optimized size and structure required to improve photothermal applications.

For nanorods, two resonance peaks corresponding to the longitudinal and transverse oscillations are observed. The resonance derived from the transverse band is weak and located in the visible range while the longitudinal resonance is strong and located in the red or NIR region (e.g., beneficial for biomedical applications since the biological transparency window is in the NIR region), showing a redshift with an increase of the aspect ratio.^[30] The longitudinal resonance is more sensitive to the aspect ratio compared to the transverse mode, which can be approximately described by the Gans theory,^[31] and recently simulated by numerical methods.^[32]

In case of non-spherical NPs, Mie theory is not applicable, and therefore sophisticated numerical approaches including finite difference time domain (FDTD), finite element methods (FEM), and DDA are needed to calculate optical properties from Maxwell's equations.^[1b,33]

FDTD is based on Maxwell's equations, which are discretized both in time and space. This method has several advantages, including a simple implementation and flexibility in terms

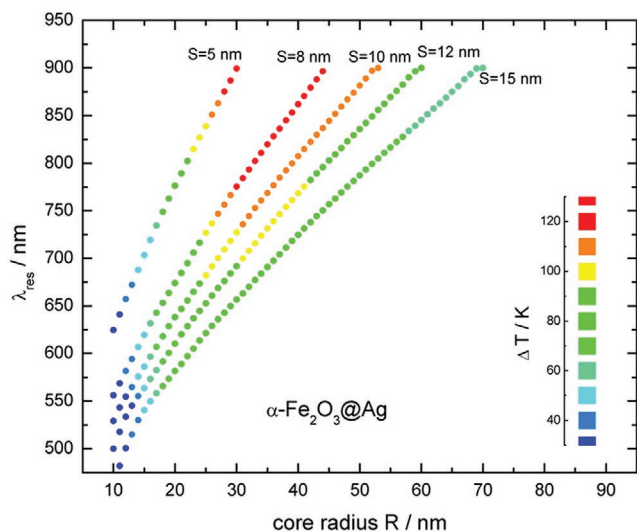


Figure 4. Resonance peak of $\alpha\text{-Fe}_2\text{O}_3\text{@Ag}$ core-shell NPs with different core radius R (in nm) and shell thicknesses S (in nm), and corresponding photothermal effect indicated by color, when dispersed in water and irradiated at their respective resonance wavelength (λ_{res}) with an irradiance of $1 \text{ mW } \mu\text{m}^{-2}$. Reproduced with permission.^[29b] Copyright 2016, American Chemical Society.

of the geometry-dependent properties, and can be applied to either 2D or 3D simulations. However, this method simulates a space domain larger than that of the NPs and requires the emulation of an infinite domain. At the same time, it may provide transient results but not steady state.

FEM is based on Helmholtz vector equations and yields approximate results at discrete points over the domain. This method is useful to accurately represent various structures and solve multiphysics problems. Compared to FDTD, this approach generates results in steady-state terms, and shows limitations for transient ones. It is more complex to implement and mesh the structure due to the simulation of a larger domain than the particle and a requirement for the emulation of an infinite domain.

Another widely used approach, DDA, is a frequency domain method derived from Maxwell's equations. The calculation is an approximation generated from the interaction between a finite array of discrete points in a continuum target. DDA is flexible in geometry and only simulates the domain of the particles. In this case, only steady-state conditions can be obtained and it is not possible to simulate transient ones. The solution accuracy shows a little improvement by adding more dipoles. Since both DDA and FEM simulate at a specific wavelength, calculations may take time for the whole spectrum.

Irregular nanostructures (e.g., nanocubes and nanoprisms), result in a more complicated interaction with light, are typically accompanied by wider peaks over a broad range of wavelengths.^[34] As shown for silver nanostructures (Figure 5), shape and geometry greatly affect the LSPR spectra.^[25] In another study, Kottmann et al. found that these resonances and associated strong fields can come from the accumulated polarization charges on the surface of plasmonic NPs.^[35] The field distribution around non-spherical nanostructures can be extremely stronger near sharp tips, suitable for near-field enhancement applications.

3.6. Composition Effects

The chemical composition of nanostructures, directly affects the interaction with light, leads to different optical properties (e.g., influencing the position and width of the resonance peaks). Noble metals, including Au, Ag, and Cu, dominate such promising properties in both visible and NIR ranges due to their intrinsic permittivity.

As a conclusion of Mie theory in the dipole approximation, the resonance happens when the real part of the metal's permittivity and the surrounding medium meets the condition $\epsilon_r \approx -2\epsilon_m$. Since the typical environment is air or water with a positive dielectric permittivity, for such NPs the negative real part is required. In addition, the imaginary part, ϵ_i , of the metal may affect the quality of plasmonic resonance peak, and it should be small at the resonance condition to confine the choice to several types of metals (e.g., Au, Ag, Cu, etc.).^[25,36] This approach works for spherical NPs, whereas the structure of nanomaterials should be taken into consideration for the most of LSPR-based applications.

To evaluate the performance of metals, it is necessary to consider not only their plasmonic efficiency and wavelength range, but also their stability. Al, Mg, In, and Ga are mostly functional in the UV region due to the high frequency of plasma, and although Li can be used for a broader region, its extraordinary activity limits any utilization.^[25,37] Therefore, Ag (narrow and intense plasmonic peaks), Au (visible to NIR plasmon range, chemical stability and inertness), and Cu (a range from red to NIR and relatively inexpensive) are the most commonly used metals for different applications in the visible and NIR region.^[34]

Alloy provides opportunities for tuning resonance by changing the permittivity through composition.^[20] There are many combinations of different metals, showing higher flexibility over pure metals. Alloy enlarges the choice of potential metals (e.g., Pt and Pd) to be combined with Au or Ag.^[38] Meunier and co-workers have developed a unique approach to synthesize Au/Ag alloy by fine controlling both composition and size.^[39] In case of alloys, since the resonance peak can be adjusted between that of the pure metals, Au/Ag alloy nanoparticles, for example, can cover nearly all visible wavelength with a proper size and dimension, enabling imaging applications.^[7b,39a,40]

3.7. The Effect of Surrounding Media

The plasmonic resonance occurs at $\epsilon_r \approx -2\epsilon_m$, which emphasizes the importance of the surrounding medium of the light interacting NPs. The surrounding medium not only determines the resonance wavelength of the electromagnetic wave and modifies the geometry of the electric field around NPs, but also affects the polarization within individual particles.^[41] The electric field resulting from oscillating electrons in the particle induces the polarization of the surrounding medium by generating charge accumulation around the interface within the particle. The accumulated charges may reduce the conduction electrons in oscillation, as larger ϵ_m results in a dramatic reduction.^[41] As a result of reducing oscillating electrons, the plasmon peak resonance can shift to a longer

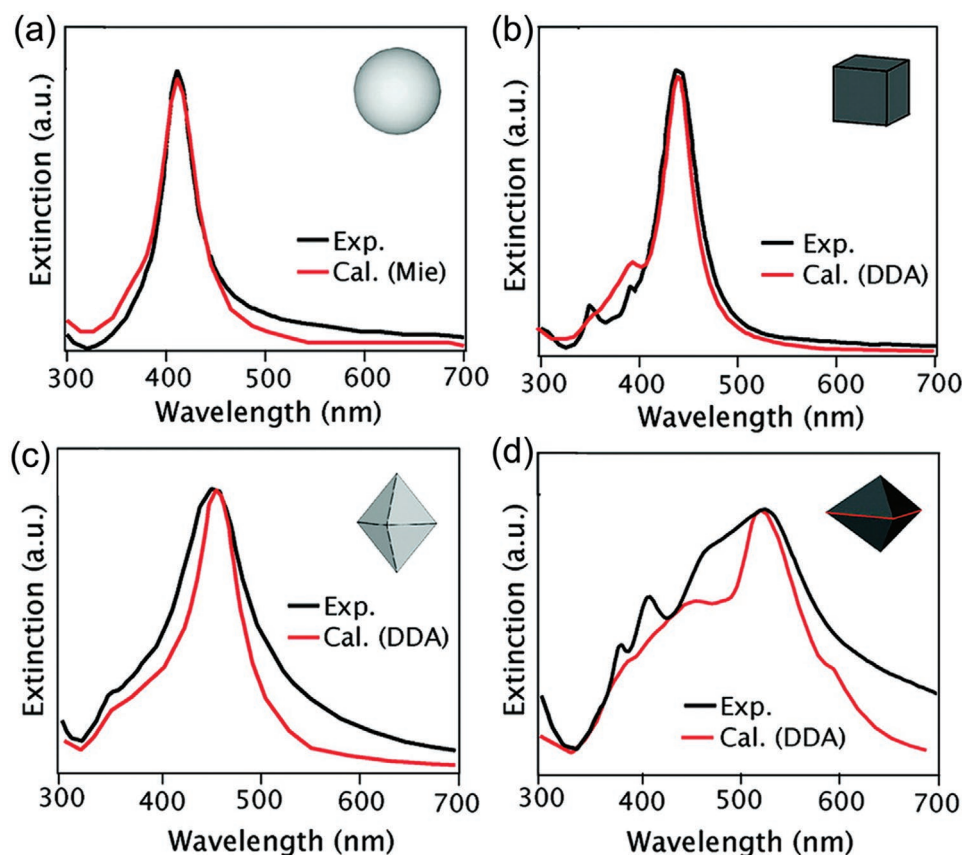


Figure 5. Experimental (black) and calculated (red) extinction spectra of AgNPs, a) spheres, b) cube, c) octahedron, d) right bipyramid. Reproduced with permission.^[25] Copyright 2011, American Chemical Society.

wavelength and the intensity of the resonance peak increases, for example, as in the dipole approximation, the absorption cross section proportional to $\epsilon_m^{3/2}$. **Figure 6** illustrates the extinction cross section and the electric field around AuNPs and AgNPs (60 nm in diameter) imbedded in surrounding media with different RI calculated by using NFMie program (Mie theory).^[26]

Based on the effect of the surrounding medium on plasmonic properties of NPs, multiple metallic and dielectric materials can behave as a surrounding medium to enhance and adjust plasmonic peaks. Indeed, a dielectric core and multilayer materials with different permittivities have been designed and synthesized to obtain specific plasmonic properties.^[42] Nanomatryushka, a multiple nanoshell, is an interesting structure showing an enhanced plasmonic peak.^[43] Silica is typically involved in the core or certain layers within the structure as dielectric spacers. Such nanostructures enable a way to control the resonance peak and its amplitude by playing with the “medium” within the NPs, without changing the size of particles. NPs are also required to be stabilized by using capping agents, such as different molecules and polymers in order to be suitable for real physiological and physicochemical situations. The capping agents strongly affect the surface plasmon of NPs (e.g., resonance peak shift, amplitude increases or decreases, as well as the accessibility and effectiveness of the field enhancement) by changing the medium permittivity that significantly influences the performance of application-oriented plasmonic NPs.^[3a,44]

4. Applications of Plasmonic NPs

LSPR phenomenon causes strong absorption and scattering effects at the resonance frequency near the NPs surface and triggers the generation of particular physiochemical features suitable for advancing a wide range of cutting-edge applications. Other than the optical cross sections, LSPR also creates a great field enhancement, which improves Raman and fluorescent signals. All these specific plasmonic properties, exploited in the field of biomedical, energy, catalysis, and information technologies, are summarized and comprehensively discussed in this section.^[3d,45]

4.1. Biomedical Technology

4.1.1. Absorption-Based Applications

The absorption cross section of plasmonic NPs dramatically increases the localized energy absorption and directly generates thermal phenomena associated to the surface plasmon.^[17a,30a] The strong absorption of plasmonic NPs induces different fascinating effects (e.g., a local temperature rise, acoustic wave, and bubble formation), which lead to new clinical theranostic techniques.^[46]

Hyperthermia: Irradiation of plasmonic NPs at their resonance wavelength can cause a local temperature rise suitable

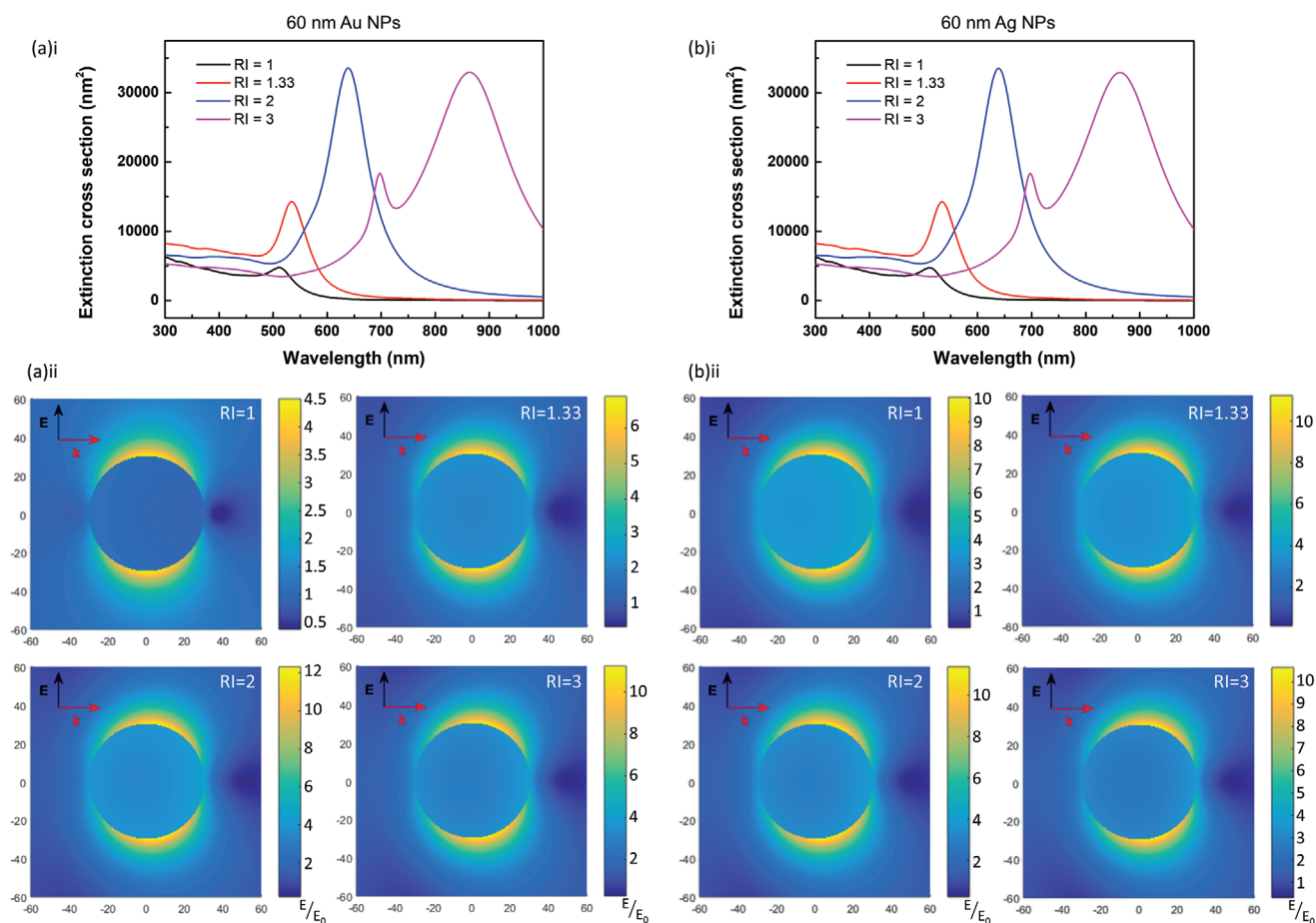


Figure 6. a-i,b-i) Calculated extinction cross section and their a-ii,b-ii) electric field enhancement of NPs at extinction resonance for 60 nm AuNPs and AgNPs in media with different refractive indices (RI) as given in the legend. Calculations done by using Rioux and Meunier's developed NFM program.^[26b]

for a wide range of therapies. Hyperthermia is a non-invasive approach owing to the generation of a confined thermal effect around the irradiated NPs and high thermal contrast between NPs and tissue. With a surface functionalization (e.g., biomolecule and ligand conjugations), NPs can selectively target specific abnormal cells, and generate an effective thermal gradient on the cells to influence cellular activity and integrity. With an intense irradiation, the temperature rise of the cellular binding NPs can destroy the target cells by melting membrane and destructing the cytoskeleton and the nucleus, and cause an intracellular release of biomolecules and protein denaturation.^[47] Due to the effective thermal contrast caused by the irradiated NPs, the intensity of laser light required for the hyperthermia of abnormal cells can be minimized to avoid any unnecessary damages to surrounding healthy tissue. For example, AuNP-mediated nanosecond laser has been used in eliminating retinoblastoma cancer cells. The localized heat generated by using a small fluence (e.g., 20 J cm⁻² from a nanosecond laser) has shown an effective cellular death up to 80% for both adherent and floating cells without harming other normal cells.^[48] The plasmonic NPs have also been widely applied to combat and eliminate bacterial infections due to their photothermal feature. Antibody-conjugated NPs specifically

bind to the target bacteria, and after laser irradiation, the localized heating generates an efficient antibacterial effect.^[49]

Taking advantage of the deep tissue penetration of NIR laser light, plasmonic NPs with a resonance peak in the NIR region show a significant capability for clinical treatments. Certain morphologies, such as nanorod, nanoshell, and nanostar, with NIR resonance have been developed to target deep tissues with long-wavelength lasers.^[50] Plasmonic nanorods, for example, are one of the promising candidates for photothermal therapy due to their redshift resonance peak compared to the nanospheres at the similar dimension.^[51] Yeh and co-workers explored the second biological transparency window, around 1000–1350 nm with longer wavelengths than the first window (650–950 nm) by developing a rod-in-shell structure (with a dimension less than 100 nm) to cover both two transparency windows, and thus greater cancer cell killing efficiency has been gained in both in vitro and in vivo compared to simple nanorods.^[50a] Due to the minimum light loss (absorption and scattering) through tissue and biomolecules, both first and second NIR window can penetrate deeper than other wavelength ranges. Studies have explored the two biological windows in phototherapy, bioimaging, and biosensing, including field-enhanced fluorescent and Raman.^[52]

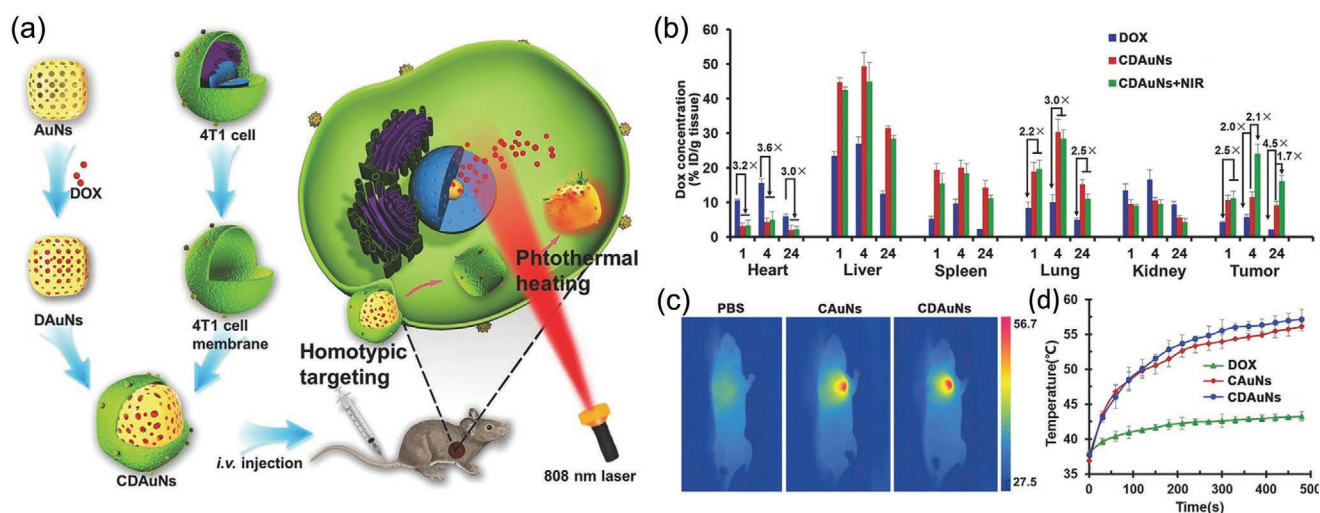


Figure 7. a) Schematic describing drug loading and cancer cell membrane-coating of Au nanocage for the hyperthermia-triggered release of DOX and in vivo treatment of breast tumor. b) Quantitative DOX distribution analysis in vivo after 1, 4, and 24 h post-injection, c) infrared thermographic images of breast tumor bearing mice with different injection (PBS, cell membrane of 4T1 cells-coated Au nanocages (CAuNs), cell membrane of 4T1 cells-coated DAuNs (CDAuNs)), and d) temperature increase of the tumor tissues in vivo with injection of DOX, CAuNs, and CDAuNs under NIR irradiation. Reproduced with permission.^[54a] Copyright 2016, John Wiley & Sons, Inc.

Highly localized photothermia effects based on plasmonic absorption in NIR region have been tested in human. Rastinehad et al., applied Au-silica nanoshells, with NIR absorption, in photothermal treatment for localized prostate cancer. In the clinical trial, they reported safe parameters and high-efficient results with plasmonic NPs infusion and focused laser ablation in human.^[53] Au-silica nanoshells in the treatment provide highly localized hyperthermia to control prostate cancer while avoiding the deleterious side effects. The pilot clinical trial demonstrated safety and efficiency of photothermal cancer treatment based on plasmonic NPs applied in human.

Photothermal effects have been elaborately adapted to generate a local stimuli-responsive therapeutic release. Chemotherapeutic molecules assembled in nanoshells, nanocages, or porous plasmonic NPs can precisely be released at the target tissue using a laser light at the corresponding plasmon resonance.^[54] The generated local heat on the irradiated NPs can induce a phase transition or degradation of chemical linkers (e.g., polymers and micelles) on the surface of nanocarriers, thus releasing the bound cargos. **Figure 7a** illustrates the process of drug loading into Au nanocage, cancer cell membrane coating, and anticancer drug doxorubicin (DOX) release triggered by NIR irradiation for a homotypic targeting and treatment in vivo.^[54a] DOX was initially loaded in the porous Au nanocages (DAuNs), then coated with the cell membrane of 4T1 cells (CDAuNs). Afterward, the prepared CDAuNs (nanocarriers), which were injected into mice adapted with the breast cancer, selectively targeted the tumor cells through the homotypic targeting. Quantitative analysis of DOX distribution in vivo has been performed at 1, 4, and 24 h after the injection (**Figure 7b**). NIR laser (at 808 nm) irradiated the NPs generated the photothermal heating and the stimuli-triggered drug release locally in the tumor site (**Figure 7c,d**). In fact, the cell membrane coating on the plasmonic nanocarriers promoted a site-specific targeting in tumor for treatment in vivo. The thermal-responsive capping by using the cell membrane also

improved biocompatibility, reduced the therapeutic leakage in the physiological environment, and decreased the drug releasing temperature to 43 °C, achieving a synergy of thermo- and chemo-therapy with a precise spatiotemporal control.

Plasmonic NPs, especially those carriers with a NIR resonance (e.g., nanocages, nanorods, nanostars), have a leading advantage over other materials, such as carbon-based or polymer-based nanomaterials, for cancer therapy due to the localized hyperthermia effect for release control and thermo-therapy. Loading capacity may become a limitation for solid plasmonic NPs, because of the high density of metal NPs; however, the fabrication of porous nanostructures as well as the selectively local release effect can make up for that, to gain higher efficiency in chemo- and thermo-therapy.

Photoacoustic Imaging: Photoacoustic phenomenon is one of the functional approaches for deep-tissue high-resolution bioimaging.^[7e,55] Since ultrasound wave has longer wavelength compared to that of the optical signal, it can easily penetrate into deep tissues without the degradation.^[56] However, the use of ultrasound without the contrast agents, such as metallic NPs, can only reflect the mechanical properties of the target tissue due to lack of the optical contrast.^[57] Plasmonic NPs owing to their strong absorption of the incident light, the temperature of and around the targeted NPs can rapidly increase, thus generating an acoustic wave during the heat transfer. The triggered acoustic signal can be subsequently detected from the body surface (superficial skin layer) by ultrasonic transducers and converted to high-resolution images. In most cases, short pulsed lasers have been employed to generate transient thermal expansions from the local area of NPs at the tissue, as a photoacoustic excitation caused by a thermoelastic expansion.^[58] Placing the ultrasound transducers near the target tissue can freely receive the acoustic signals reaching the body surface, and the images can be constructed with the distribution and intensity of the light absorption. On the other hand, the use of detectors at different locations from the target tissue can elaborately generate

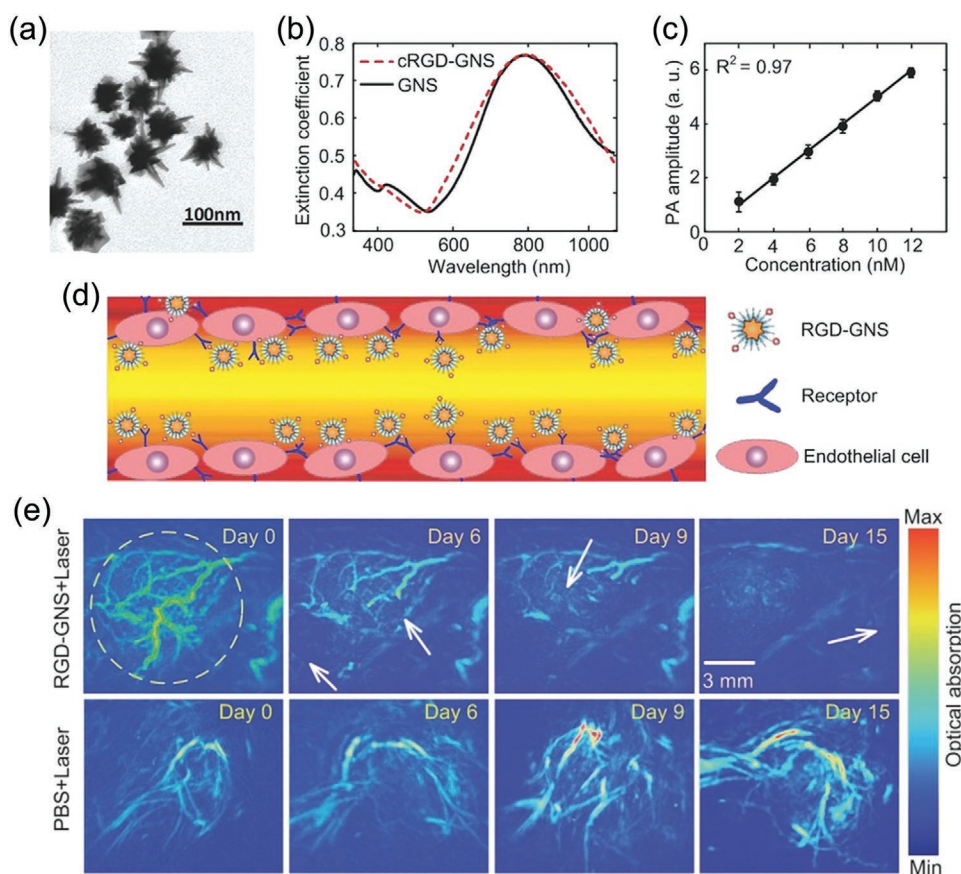


Figure 8. a) TEM image of gold nanostars (GNS), b) extinction spectra of GNS and RGD-GNS, with peak at ≈ 790 nm, and c) experimental relation between photoacoustic (PA) amplitude and concentration of NPs. d) Schematic of RGD-GNS specifically targeted on endothelial cells. e) Photoacoustic images for therapy monitoring in 15 days with Au nanostars and PBS injection. The white arrows in figure (e) point out the obvious changes after treatment with RGD-GNS. (RGD-GNS: Cyclic Arg-Gly-Asp (RGD) peptides conjugated plasmonic gold nanostars; PBS: phosphate-buffered saline). Reproduced with permission.^[61] Copyright 2013, John Wiley & Sons, Inc.

the photoacoustic tomography accompanied by complexed structures. The intensity of the photoacoustic signals, which are proportional to the heat generated by the absorption of electromagnetic wave, can be adjusted to facilitate high-resolution 2D and 3D image processing.^[56,59] Photoacoustic phenomenon is an interesting approach in high-resolution bioimaging obtained by the combination of the ultrasound and differentiable contrast given by cellular binding plasmonic NPs.^[7e,55]

Au nanostructures as photoacoustic contrast agents have been applied for cancer diagnosis, brain vasculature and function, as well as the image-guided therapy.^[60] Among which, Au nanostructures accompanied by the NIR resonance (e.g., nanorods, nanoshells, nanoprisms, nanostars, and nanocages) are preferable for visualizing deeper tissues by using elaborated photoacoustic devices. For example, Au nanostars with a tunable NIR resonance can also improve the contrast of photoacoustic imaging (Figure 8).^[61] Post-fabrication with cyclic Arg-Gly-Asp (RGD) peptides has shown a great potential for targeting of endothelial cells with overexpressed integrin $\alpha_v\beta_3$, which associates with neovessels in tumor. The gold nanostars (GNS), prepared with an extinction peak ≈ 790 nm, interestingly keep their intrinsic optical properties after the functionalization with RGD peptides as well. Therefore, the specific targeting and

high photoacoustic contrast enabled RGD-GNS to improve the quality of photoacoustic imaging by providing high specificity and sensitivity. Meanwhile, the absorption of plasmonic NPs at the resonance largely enhances the localized photothermal effect that may be used for tumor treatment (Figure 8e). This elaborate development of multifunctional plasmon-based nano-materials demonstrates great potential in theranostics due to the high contrast created by site-specific cellular binding NPs over the target tissue, as well as precise localized photothermal therapy. Besides nanostars, nanorods have been widely applied in photoacoustics as contrast agents.^[62] Ultra-small Au nanorods coated with an organic dye (IR780) and anticancer drug DOX have also shown their ability to enhance photoacoustic and therapeutic effects.^[55c] Therefore, the imaging contrast agent (e.g., plasmonic nanostars as an “on-spot” theranostic platform) helps to detect and identify the target tissues for performing an effective therapeutic hyperthermia, which only omits the cancer cells without inducing side effects to healthy organs.^[61]

Optoporation: Transfection is an alternative effective approach for disease treatments. The optical transfection, known as optoporation, triggers a mild cellular perforation to directly deliver therapeutics into the cytoplasm of the target cells. This optical approach (physical) illustrates certain great advantages over

other non-physical transfection strategies (viral and non-viral) due to the high transfection rate and less toxicity.^[63] Photostability and their ability to be functionalized with biomolecules and ligands allow plasmonic NPs specifically attach to targeted cells for the optoporation. Compared to other physical approaches (e.g., mechanical and physical transfection) limited for gene delivery *in vivo*, plasmonic properties combined with the pulsed laser realize optoporation as the most precise and accurate transfection method *in vivo*; however, it still needs attention for improving the transfection of deep tissues. High compatibility with optical microscopy, as well as the possibility of focusing beam on the layer of interest and employing short pulse, optoporation can be performed in a real time accompanied by the control and precision.^[64] Since the physical disruption of the lipid bilayer of cellular membrane does not activate immune responses compared to that observed from the administration of viral vectors, optoporation can avoid the immunogenicity problems.^[65]

Taking advantage of their corresponding practical responses to the incident light, plasmonic NPs-assisted laser optoporation and perforation have been developed for the transfection of living cells. A weakly focused laser irradiation of cellular binding plasmonic NPs on targeted cells can transiently permeabilize the lipid bilayer of cellular membrane and facilitate the internalization of exogenous molecules (e.g., drugs, oligonucleotides, proteins, and plasmids).^[46a] A short pulse laser irradiation (e.g., picosecond or femtosecond laser) can generate a rapid temperature raise, followed by the formation of nanobubbles around plasmonic NPs.^[65,66] This bubble formation process can precisely cause transient, highly localized holes on the cell membrane close to the irradiated plasmonic NPs, thus allowing various exogenous biomolecules to be delivered into target cells.^[63,67]

In the early stage, fluorescent dyes (e.g., calcein, propidium iodide, and fluorescein isothiocyanate -dextran, etc.) have been frequently employed to analyze permeability mechanisms of the targeted cell membrane and improve the cellular transfection.^[68] AuNP-mediated picosecond laser optoporation, for example, has been found highly practical due to achieving a therapeutic level (up to 88% *in vitro*) of transfection efficiency (fluorescent labeled siRNA) into canine pleomorphic adenoma ZMTH3 cells with maintaining high cell viability (over 90%).^[69]

Non-specific optoporation, conducted by a simple and random sedimentation of plasmonic NPs on the cells (*in vitro*), has truly shown inefficient therapeutic effects, and therefore an elaborated surface functionalization by means of antibodies and other biomolecules needs to be developed in order to obtain site-specific therapeutic delivery.^[69] To achieve therapeutic effects, Meunier and co-workers, for example, have developed anti-CD44 functionalized AuNPs for a selective perforation of MDA-MB-231 breast cancer cells under femtosecond laser irradiation (at 800 nm) to analyze involving mechanisms for an effective site-specific therapeutic delivery. Polyethylene glycol as a bifunctional linker (thiol and N-hydroxysuccinimide ester) can bind functional antibodies and anchor them on the surface of the plasmonic NPs. In this case, Ab_{CD44} functionalized NPs bound on the cellular membrane of MDA-MB-231^{CD44} and ARPE-19^{CD44} cells 150 times more than that of 661W^{CD44} cells, and enabled a successful selective optoporation without influencing other cells in the co-culture.^[44b]

Taking advantage of site-specific therapeutic delivery for future clinical translation, Meunier and co-workers have demonstrated an effective femtosecond laser optoporation of retina (*in vivo*) by using K_v1.1-functionalized AuNPs (100 nm in diameter) to deliver Cyanine 3-tagged siRNA (a scramble fluorescent labeled siRNA) to retinal ganglion cells without reducing their cell viability (**Figure 9**).^[7a] In this case, an intravitreal injection assisted the delivery of functional AuNPs and fluorescent labeled molecules (siRNA or fluorescein isothiocyanate-dextran) to the target retinal tissue. The optical path (**Figure 9b**) was administrated for the optoporation *in vivo*, with a femtosecond laser at 800 nm, locally focused on the retina (ganglion cells) of rat (**Figure 9c,d**) incubated with the pre-injected functional AuNPs and biomolecules. The results certainly prove the successful functionalization of NPs that a large number of these well-distributed NPs bound on the targeted retina tissue/explant (**Figure 9e,f**). Significant efforts are still being put to achieve the highest therapeutic effects via plasmonic NPs-assisted optoporation by reducing the fluence threshold for the unharmed bubble formation *in vitro* and *in vivo*.^[67b,70] A theoretical model has been also developed to simulate the effects of different kinds of plasmonic nanostructures participated in the optoporation. For example, silica-Au core-shell NPs designed as one of the effective nanostructures, which lowered 51% of the cavitation threshold at the NIR irradiation (at 800 nm) compared to that of the homogeneous AuNPs.^[70] The nanoshell composed by SiO₂ core (42 nm radius) and Au shell (29 nm thickness) was theoretically determined and experimentally verified as an optimum nanostructure, which reduces the cavitation threshold to $\approx 35 \text{ mJ cm}^{-2}$.^[67b] This non-invasive optoporation technique may lead to an efficient cell-specific therapy in clinics.

4.1.2. Scattering-Based Applications

Light scattered from plasmonic nanoparticles of different composition, geometry and composition may be collected and analyzed for different types of biomedical applications. In addition, the light propagation due to the scattering cross sections of plasmonic NPs can also be manipulated at the nanoscale range to provide unique opportunities for specific biomedical applications. Moreover, the use of different nanostructures and surface modifications (e.g., antibodies, ligands, and peptides, etc.) can generate an alternative robust protocol in order to produce high-efficient biosensing and bioimaging devices. Biocompatibility and specific targeting are highly required in these applications, and thus substantial attentions have been paid to design elaborated surface modifications for creating highly stable imaging contrast agents.^[44b,71] For example, heterobifunctional polyethylene glycol is one of the widely applied polymers effectively reducing nonspecific cellular adsorption and aggregation of plasmonic NPs and improving their biocompatibility for a broad range of bioimaging and biosensing applications.^[44b]

Bioimaging and Diagnosis: The role of plasmonic NPs as promising contrast agents has been thoroughly proven for bioimaging and detection of cancer cells and cellular biomolecules (e.g., expressed proteins and antigens, etc.) due to their large scattering cross sections, high-resolution, and chemical- and

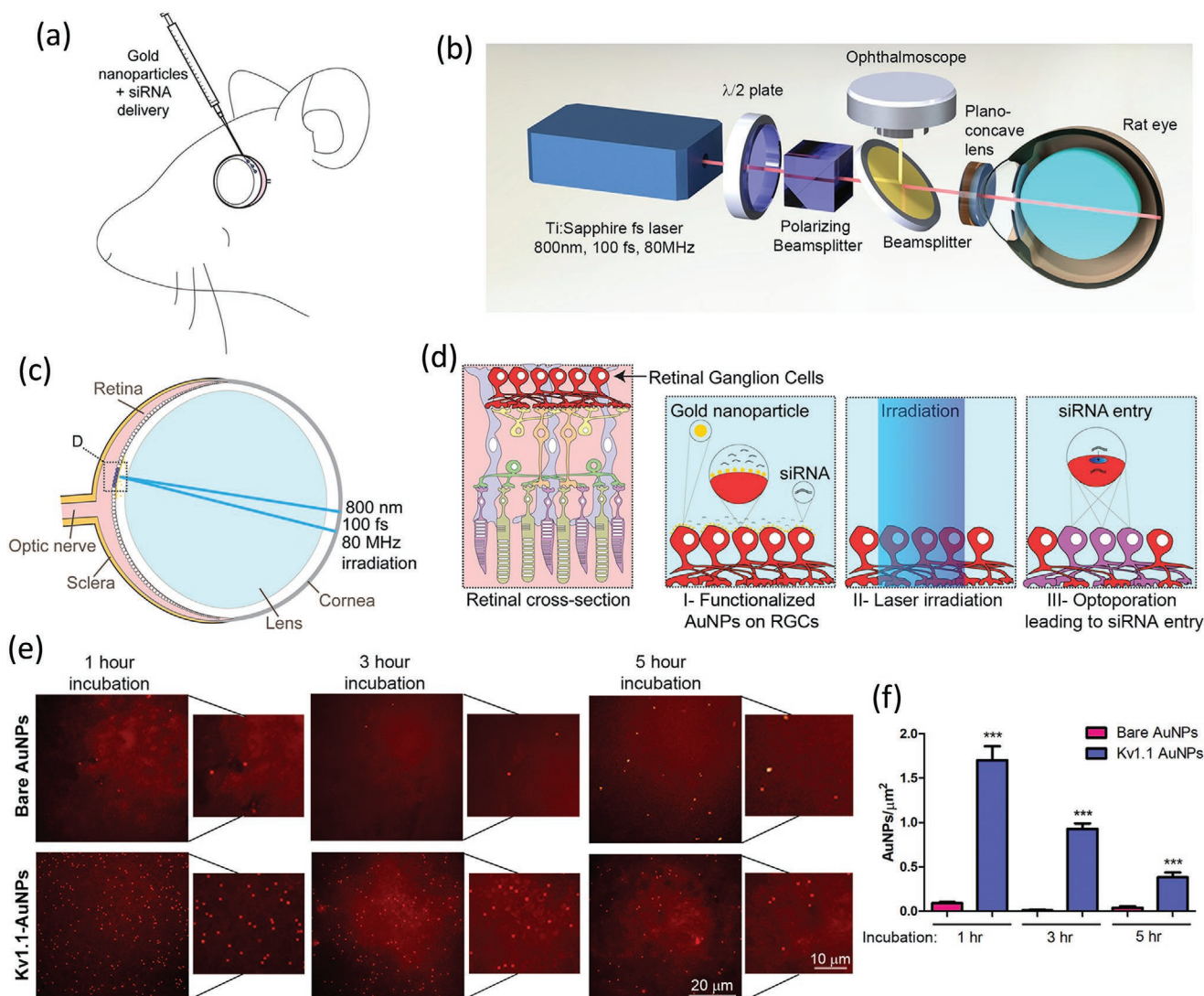


Figure 9. AuNP-mediated femtosecond laser irradiation for in vivo treatment of retina cells. a) Schematic of the injection of NPs and siRNA to the back of the eye in vivo, b) optical setup for femtosecond laser optoporation, c) laser-beam path in the eye, and d) detail of NPs targeted to retinal cells at different steps during the treatment. Cell membrane binding and distribution of bare and $K_v1.1$ functionalized AuNPs on retina explants e) visualized and f) quantified under an enhanced dark-field microscopy at different incubation periods. Reproduced with permission.^[7a] Copyright 2018, American Chemical Society.

photo-stability compared to traditional fluorescent agents.^[72] The strong scattering generated by the interaction with the incident light even makes plasmonic NPs visible under normal optical microscopes (e.g., dark field and back scattering mode), and this promising feature can be elaborately employed to simply create a quantitative multiplexing imaging process.^[73] The stable and strong scattering signal from the plasmonic NPs easily enables the fabrication of highly sensitive and cost-effective bioimaging and biosensing devices, desperately needed in clinical diagnosis and therapeutic monitoring.

In case of bioimaging, scattering signals from plasmonic NPs are composition- and shape-dependent and adjustable for obtaining different intensities and colors. The plasmonic NPs with different chromatic spectra can facilitate a multiplex imaging system as contrast agents.^[7b,74] For example, Au/Ag alloy NPs are one of practical contrast agents providing a range

of tunable chromatic spectra by adjusting their composition and size and improving current multiplex imaging systems. As shown in **Figure 10a**, the composition of the spherical alloy NPs (at the same size range) has been precisely adjusted from pure Ag to pure Au, resulting in different extinction spectra.^[39a] The Red-Green-Blue (RGB) illumination and scattering spectra of NPs for different media are shown in **Figure 10b**. **Figure 10c,e** shows breast cancer cells labeled with specifically designed plasmonic NPs for RGB (blue: 10:90 Au/Ag, green: 50:50 Au/Ag, and red: Au nanorod) under a dark-field optical microscope in different mediums (PBS, mounting medium and oil).^[7b] Scattering spectra from plasmonic NPs have also been applied in hyperspectral imaging, providing more detailed spectral information for a quantitative analysis.^[40,75] Furthermore, a large number of nanostructures, composed of pure metals and their alloys, have been developed to specifically scatter light at the

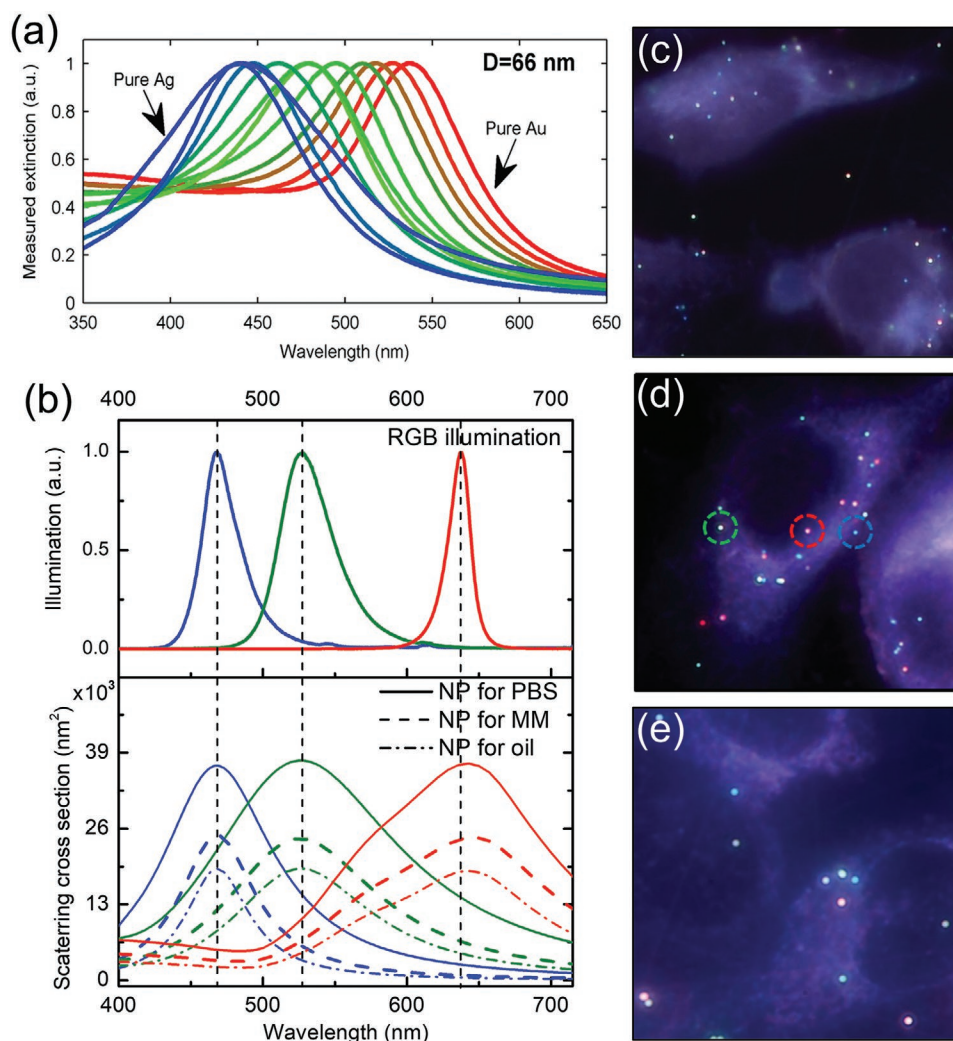


Figure 10. a) Extinction spectra of Au/Ag NPs of different composition. Reproduced with permission.^[39a] Copyright 2015, American Chemical Society. b) The RGB (red-green-blue) light source spectrum and theoretical scattering cross section of Au/Ag NPs designed for the illumination in phosphate buffered saline (PBS), mounting medium (MM), and microscope immersion oil for a dark field bioimaging. The representative dark-field side-illumination images of Au/Ag NPs (Red, green, and blue scattering light) on the cell membrane in c) PBS, d) MM, and e) the immersion oil. Reproduced with permission.^[7b] Copyright 2019, John Wiley & Sons, Inc.

NIR resonance for a high-resolution deep tissue bioimaging.^[76] Besides cells, the use of functionalized plasmonic NPs enables a quick recognition of viral organisms and other pathogens under darkfield microscopy.^[77]

An elaborate combination of differentiable scattered lights (RGB colors) as well as specific cellular binding features (surface functionalization) of plasmonic NPs can be further used in many applications in bioimaging, diagnosis, and therapy.^[5b,78] Scattering lights from functionalized plasmonic NPs can provide a facilitated chromatic way to substitute current complex diagnostic strategies in regard to the common detection kits (e.g., pregnancy, cancer, and infection). With the development of metallic NPs, typically AuNPs and others (e.g., Ag, Pt, and Pd, etc.) by employing a specific surface functionalization (e.g., antibodies, peptide, and aptamers), these functional plasmonic NPs can be assembled as a rapid and sensitive detection kit for a wide range of diseases.^[79] Even

with such progresses, critical challenges are being addressed in terms of signal intensity, penetration depth, and resolution needed to be thoroughly considered before moving toward clinical translation.

Biosensing: LSPR is highly sensitive to the refractive index near the surface of plasmonic NPs, strongly influencing the LSPR peak, and the phenomenon can be served to improve spectral sensors. Due to easy surface modification of plasmonic NPs with biological and chemical molecules as receptors, the spectral sensors can selectively detect analytes and precisely report plasmonic peak shifts or broadening as a definite response.

Both single and assembled plasmonic particles can be implemented for the construction of a platform as a biosensor with a tunable feature based on the intrinsic morphology and composition, as well as the refractive index of surrounding medium.^[80] Particle's size shows a direct impact on the detection spectrum

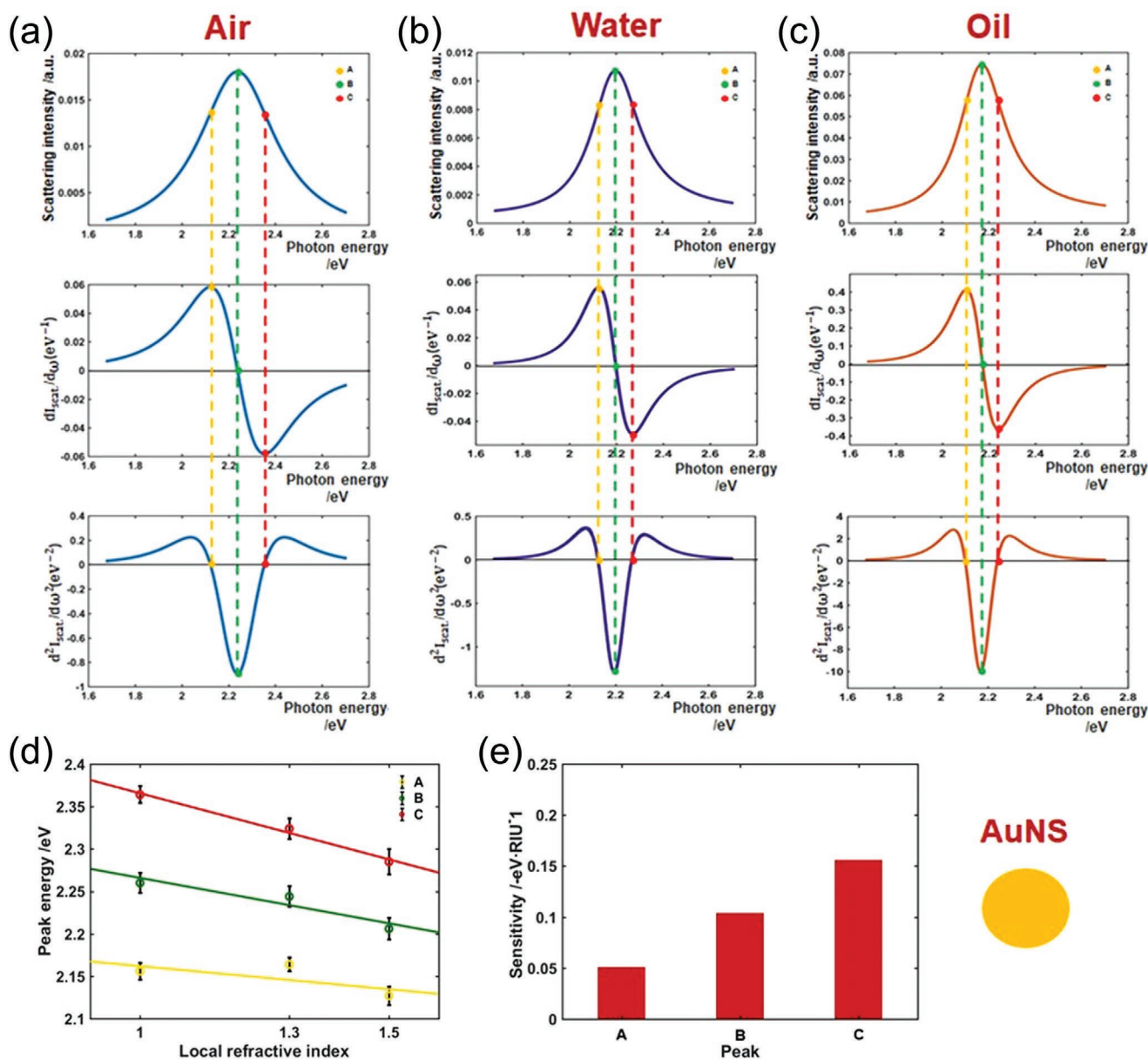


Figure 11. Extinction spectra (first row), their first derivative (second row), and second derivative (third row) of Au nanosphere (AuNS) in a) air, b) water, and c) oil. The inflection points indicated with dash lines as A (yellow dashed line), B (green dashed line), and C (red dashed line). d) Peak energy dependence on the local refractive index at the inflection points. e) The sensitivity to refractive index at the inflection points. Reproduced with permission.^[80] Copyright 2019, Springer Nature Limited.

range. An ultra-sensitive plasmonic platform can therefore be obtained by using smaller particles (due to their small local volume), while bigger particles in diameter can be assembled to detect analytes on a wider spectral range. In fact, smaller particles can mostly be influenced by the absorption, while the larger particles by scattering features, and both size ranges can facilitate a precise analysis for the detection of analytes through the extinction spectrum. The light-matter interaction (based on plasmonic NPs) can confine the detection range to an ultra-thin layer near the surface of the particle to provide a local supersensitive lab-on-a-chip device working at a very low concentration of analytes.^[81]

Traditionally, plasmon peak shift is the main tracking point to evaluate the detection sensitivity, but these plasmon responses are subjected to lose their sensitivity due to an unsymmetrical broadened spectrum. In this case, the refractive index-based sensitivity can be improved by evaluating the shift of the inflection points origin from the second derivative of the extinction spectrum, because the inflection point at the longer wavelength region with a similar refractive index change enables a noticeable shift (Figure 11).^[80] By using the inflection point method, different types of AuNPs (e.g., nanospheres, nanorods with different dimensions, and nanostars) are able to improve bulk refractive index (RI) sensitivity around 18–55%.^[82] Based on a

similar method, the refractive index sensitivity of single AuNP is also found to be shape-dependent. The plasmonic NPs with sharp vertices and edges (e.g., nanocubes compared to nanospheres of same size range) possess higher RI sensitivity.^[80] Instead of the inflection point, a curvature of the extinction peak can also be employed to improve the signal-to-noise ratio and the reliability of LSPR sensors by eliminating instrumental noises.^[83] Plasmon-based bioimaging and biosensing rely on structural features of plasmonic NPs, substrates, as well as data analysis strategies. To achieve ultra-sensitive and accurate plasmon-based biosensing devices, our knowledge as a proof-of-concept regarding plasmonic properties certainly needs to be developed in order to accelerate a quick and accurate data analysis and affordable clinic translation, as well as other regulations required to facilitate their utilization in everyday life.

4.1.3. Field Enhancement Applications

The field enhancement effect enables a passive bioimaging and detection by enhancing the emission signal from the emitter, placed in the near field of targeted plasmonic NPs. The field enhancement provides opportunities for an ultra-sensitive detection, even at the molecular level. Among various types of signals, Raman- and fluorescent signals are the most advanced spectroscopic and microscopic strategies, developed for the field enhancement detection and imaging.

Surface-Enhanced Raman Spectroscopy (SERS): Since initially observed in 1973 by Fleischmann, SERS has attracted lots of attention due to the dramatic enhancement of Raman signals, thus achieving an ultrahigh sensitivity in the detection of small molecules.^[84] Taking advantage of plasmonic field enhancement that may reach up to four orders of magnitude in certain nanostructures, Raman signals can remarkably be enlarged by 10^8 to even 10^{15} , opening up the possibility to detect single molecules.^[85] The molecular specificity of Raman spectroscopy combining with the surface plasmon resonance from plasmonic NPs can generate highly sensitive “fingerprint” SERS platforms.^[45b] SERS-based platforms mainly involve two basic mechanisms for the signal enhancement. The most privileged mechanism is based on the influential electromagnetic mechanism caused by the concentrated electric field in the LSPR around plasmonic NPs (e.g., Raman signal enhancement up to 10^{10}). The second mechanism with a much smaller enhancement feature (e.g., up to 100) is attributed to the chemical enhancement caused by an interaction between molecules and NPs.^[25,45b]

SERS based platforms are highly sensitive and responsive to the geometry of implemented nanostructures (e.g., sharp angles and clusters) in which plasmonic hot spots with large near-field enhancements can be used for the low concentration molecular detection.^[86] According to both experimental and modeled field enhancement effect of plasmonic NPs, the highest enhancement comes from three types of nanostructures, including I: gaps, II: tips, and III: crevices. Therefore, many nanostructures transcend spherical ones, including nanocubes, nanoshells, nanosponges and other assemblies, which harvest gaps between each individual particle and their clusters.^[87] **Figure 12a** illustrates the simulation of the resulted field

enhancement between a pair of AgNPs, irradiated by a polarized light, and indicates the gap between the pair of particles with the highest field intensity. For example, a well-designed porous structure consisting of AgNPs embedded in silica coating around Au nanorod (Figure 12b) was used to gain a quantified SERS signal of probing molecules (1,2-bis(4-pyridyl) ethylene) at different concentrations (Figure 12c).^[88] Following the same concept, Köker et al. designed SERS “hot spot” by coupling a pair of AuNPs between deposited an activated Raman reporter to be specifically differentiated. This tiny gap around 2 nm created between the two particles can enable the highest SERS signal emits from the green fluorescent protein for a cellular bioimaging and spectral sensing (Figure 12d–f).^[7e] Due to the sensitivity and extremely small volume of the field enhancement, assembling Raman reporters into the hot spots is critical in order to generate a reproducible and controllable enhanced signal.

An elaborated assembly of plasmonic nanostructures, including disordered nano-islands formed by nanoaggregates and close-packed mono- or multi-layers of nanospheres, provides high performance SERS substrates required to generate a highly sensitive platform for the detection of chemical and biological analytes.^[89] However, the reproducibility of the high performance SERS substrates privileged by the assembled plasmonic nanostructures has been an engineering challenge, prohibiting a wide range of sensing applications. To fabricate the sensitive SERS substrates, thermally or electrokinetically driven deposition of aggregates can be a practical approach in order to control the disorder degree of these assemblies compared to the other techniques (e.g., flame spray pyrolysis and magnetron sputtering deposition).^[89a,90] The control and optimization of fabrication parameters during the assembly of plasmonic nanostructures can directly contribute to the generation of hot spots of different densities, and facilitate a cost-effective production and utilization of the ultrasensitive SERS platforms. Compared to the disordered assemblies, the well-designed SERS substrates, for example, covered by a closed-packed nanospheres layer (with an optimized diameter and interparticle gap) shown a narrower plasmonic peak, sustain way better predictable field enhancement properties, influencing the enhance factor of the detection technique. Based on close-packed plasmonic NPs mono- and bilayers, the theoretical calculation exhibits enhancement factor up to 10^7 and hot spots density up to $1000/\mu\text{m}^2$. The theoretical outcomes together with well-developed synthesis techniques confirm the potential of plasmonic assembled nanoarrays for SERS applications.^[89b]

DNA origami technology, besides the above-mentioned approaches, is able to generate an accurate spatial assembly of plasmonic NPs in a large-scale (up to 500 nm) with the sub-nanometric precision, important for designing application-oriented plasmonic properties.^[91] With the structure programming, DNA origami technology shapes a reproducible and biocompatible scaffold, which precisely controls the distance and angle among the assembled plasmonic NPs. Wang et al. created reconfigurable diastereomers with DNA origami platform for assembling Au nanorods.^[92] The complex can have up to three chiral centers, through DNA strand-displacement reaction, the L- and R-chiral center can switch from one to another,

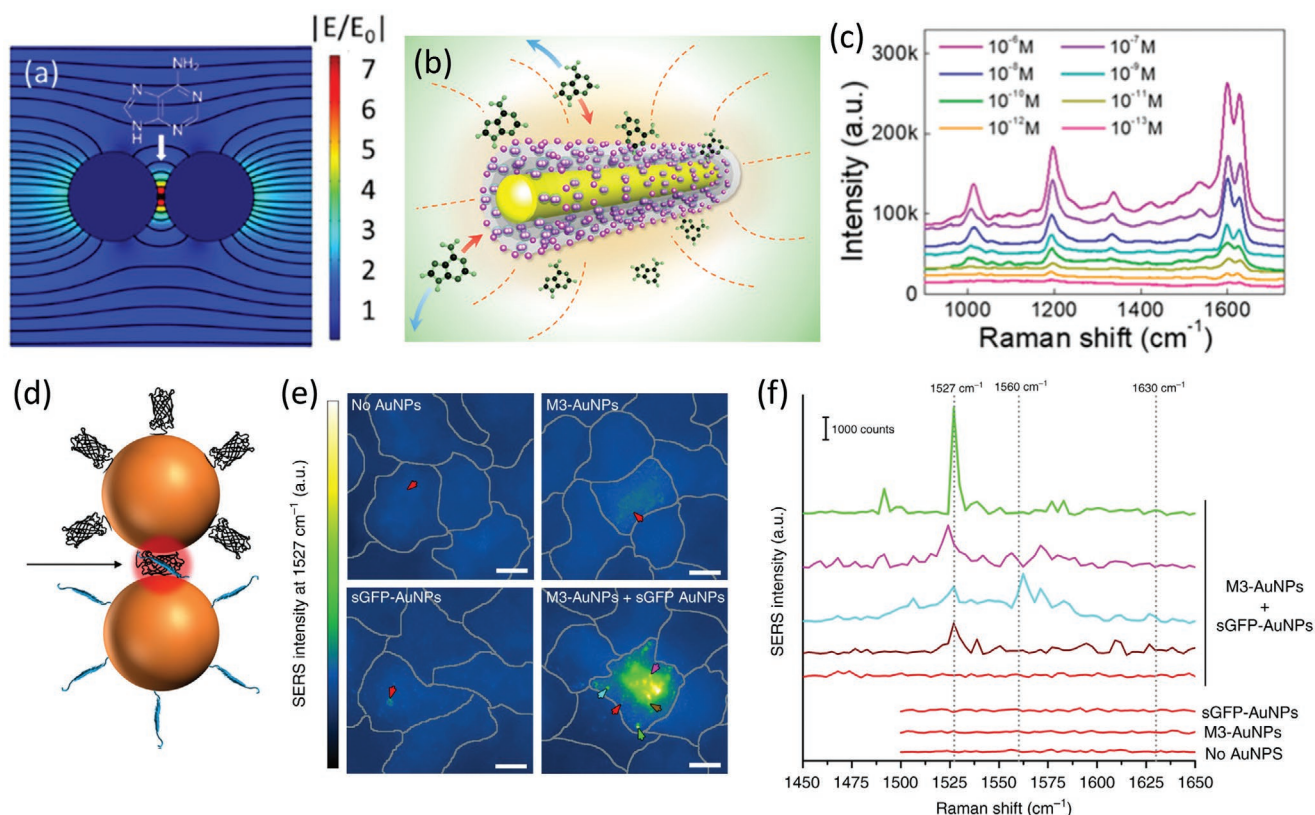


Figure 12. a) Simulation of electric field enhancement of AgNPs pair with reporter molecule at the gap, b) schematic of the sensing process with designed porous particle as Raman sensor, and c) the SERS signal of 1,2-bis(4-pyridyl) ethylene in different concentrations enhanced by the designed particles. Reproduced with permission.^[88] Copyright 2018, American Chemical Society. d) Schematic of “hot spot” created by assembling of two AuNPs through the surface function with green fluorescent protein and peptide fragments, as well as e) SERS image and f) spectra of differently functionalized NPs with peptide (M3) and split green fluorescent protein (sGFP). Reproduced with permission.^[7e] Copyright 2018, Springer Nature Limited.

displaying different circular dichroism spectra. The spatial gap is one of the most promising SERS structures due to the sensitivity of the enhancement effect to the distance between NPs. In this case, DNA origami nano-assemblies, enable a reproducible and precise gap between plasmonic NPs, offering a perfect technology to couple pairs of NPs as gap-enhanced SERS substrates. Thacker et al. created AuNP dimers with reliable sub 5 nm via DNA origami to detect SERS signals from not only external analytes absorbed molecules, but also the composition change of single-strand DNA attached to the NPs.^[93]

Both Au and Ag nanostructures have been widely studied in SERS based applications because i) Ag has the most prominent effect for the Raman enhancement in a broad spectral range (400–1200 nm) and ii) Au has valuable enhancement behavior combined with good chemical stability and biocompatibility.^[25,45a] Wang and co-workers have theoretically investigated aspects of Au/Ag hybrid nanoparticles in terms of the composition and structure to improve SERS performance. Au/Ag alloy NPs showed higher field enhancement compared to both pure Au- or Ag-based particles at the certain incident wavelength ranges (e.g., $\approx 420\text{--}520\text{ nm}$) because of the different intrinsic plasmonic peaks of pure Au and pure Ag and the peak shift effect with chemical composition change. Au/Ag nanoshells with silica core have interestingly shown a stronger field enhancement in a broader range of spectrum than all others (e.g., Au/Ag alloy,

AuNPs, and AgNPs), due to the modulation of environmental RI and variety of both chemical composition and shell thickness, and can be considered as a practical composition and structure applicable for future clinical translations.^[45a]

Due to tremendous progress in the fabrication of plasmonic NPs for SERS based platforms, it is highly possible to detect small molecules (e.g., a single nucleic acid) in the local environment of particles and tag markers on the surface of the particles to build sensing and imaging biomarkers (in vitro and in vivo).^[87a,94] For example, Olivo and co-workers tagged various SERS markers on functionalized AuNPs for multiplex detection in vivo (**Figure 13**). The peaks at 1120, 1175, and 1650 cm^{-1} are corresponding to Cyanine 5, malachite green isothiocyanate, and rhodamine 6G attached to the particles, respectively. SERS signals obtained from the treated mice (**Figure 13b,c**) indicate that the SERS markers can quickly be vanished in the control groups (the healthy organs, less than 4 h), whereas the cellular binding AuNPs stayed much longer (more than 2 days) in the targeted tumor site, detectable via the long-term emitting signals.^[95] Meanwhile, the high sensitivity SERS substrates provide a promising platform for an accurate trace detection of bacteria as a key point for the diagnosis of bacterial infections in early stages. Depending on chemical compositions, characteristic SERS signal provides information of various bacteria, and their detection.^[96]

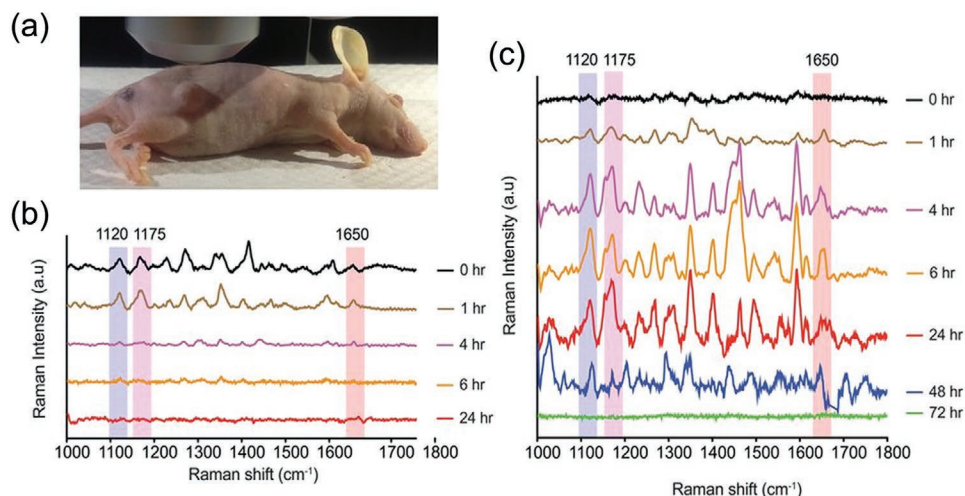


Figure 13. a) Animal model for SERS experiment for tumor detection, b) SERS spectra from tumor site in control mice with non-functionalized markers, and c) in test mice with functionalized markers. Raman spectra were taken at the tumor after different incubation periods as indicated in the legend. Functionalized markers remain more than two days after the biomarker injection. Reproduced with permission.^[95] Copyright 2014, Springer Nature Limited.

Surface-Enhanced Fluorescence: Fluorophores are widely used in biomedical applications due to their great accessibility and easy utilization. However, the deficiency, caused by their small cross section and their tendency for a quick photobleaching, dramatically influences their stability and triggers certain difficulties for a precise quantification required for a long-term diagnostic process. In this case, the use of plasmonic NPs has brought a significant improvement for both radiative and non-radiative decay of fluorophores, and altered their quantum yield and lifetime.^[45c,97] Based on the similar mechanisms involved in the improvement of SERS platforms, when fluorophores as biomarkers for bioimaging and biosensing are placed in the field enhanced region (near the surface of the plasmonic particles), the surface-enhanced fluorescence (SEF) can be obtained due to the well-known LSPR phenomenon. The emission enhancement, calculated by ηE^2 , where η is the quantum yield of fluorophore and E is the normalized electric field at the position of the fluorophore.^[98] Due to the property and stability of different fluorophores, the measured enhancement factors vary a lot for each individual experiment.^[97a,99]

The morphology of particles (due to concentrating the electric-field) and the spatial distance of fluorophore from the surface are crucial for SEF-based platforms. For example, fluorophore molecules must be slightly far away from the plasmonic NPs to avoid quenching of the signal because of a non-radiative deexcitation of the fluorophores. Fluorophores close to the surface (around 1–5 nm) can be affected by the electron transfer to the NPs, which will quench the fluorescent signal, while in the range of 6–20 nm (slightly far from the surface using spacers, such as SiO_x), the signal can be strongly enhanced owing to the field enhancement from the plasmon. As shown in **Figure 14**, Mei and Tang have taken advantages of controlled fluorescence quenching and enhancement mechanisms, depending on the distance between fluorophores and Au nanorods to analyze oligonucleotide detections. Simply, depending on the DNA paired or not (unfold or fold), the fluorescent signals will be respectively enhanced or quenched (**Figure 14b**). Taking advantage of

the tunable dimension of nanorods (varying the aspect ratio), plasmonic spectrum can be precisely controlled to reach a match with both excitation and emission wavelength of fluorophores. Moreover, the great fluorescence enhancement can omit the limitations on the DNA detection process and greatly bring an expected accuracy for quantified results (**Figure 14c**).^[7f] A simultaneous utilization of different fluorophores provides a multiplex detection with fluorescent mode. Moreover, multi-mode imaging, for example, has been developed by combining SEF and scattering light from plasmonic NPs. Plasmonic NPs with different compositions (e.g., pure Ag and Au/Ag 50:50) coated with silica containing different fluorophores (e.g., fluorescein isothiocyanate and Rhodamine B isothiocyanate) provide a dual-mode platform for multiplexing bioimaging.^[100] The combination of scatterings from plasmonic NPs and plasmonic enhanced fluorescence can significantly enlarge multiplexing opportunities by using a spectrum of biomarkers under a similar observation set up to enable quantitative analysis approaches.

4.2. Energy Technology

Solar energy is the most sustainable green energy owing to 5000-million-year lifetime and tremendous yield of about 4000 times more than that of the global electric energy consumption in the world.^[44] Therefore, many techniques, including photothermal, photovoltaic and photochemical approaches, have been developed for harvesting and converting the solar energy for various applications. One of the main challenges for a wide implantation of these developed approaches is the lack of light absorption and conversion efficiency; however, the use of metallic NPs in the energy conversion devices has shown potential to improve outcomes of these approaches.^[101] Similar to the mechanisms involved in biomedical applications, absorption, scattering and field-enhancement play roles in different energy approaches.

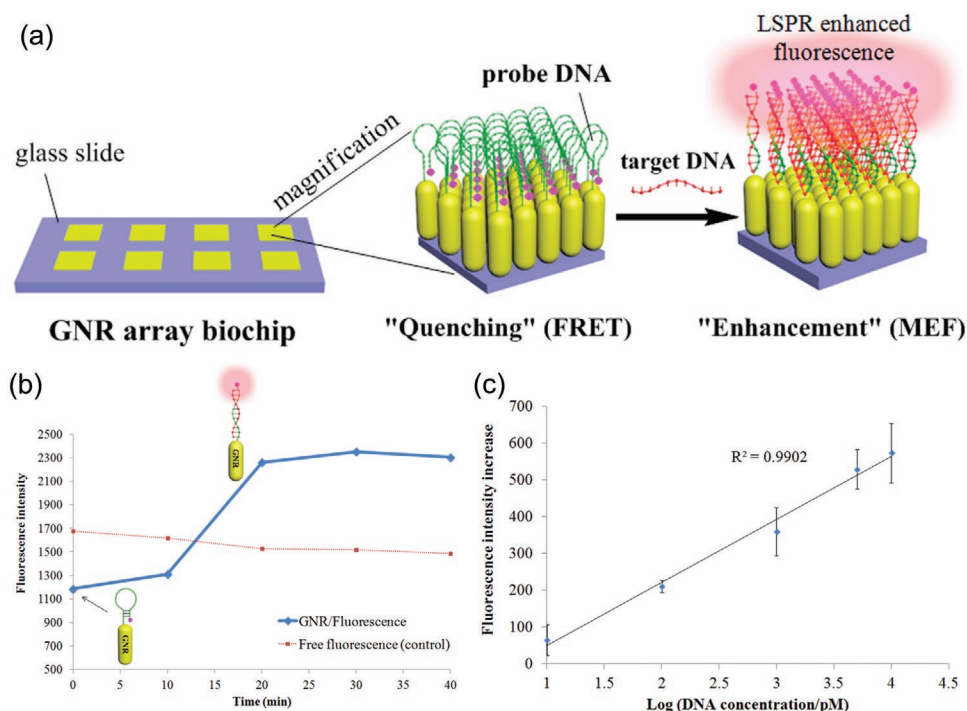


Figure 14. a) Schematic of LSPR enhanced fluorescence applied in Au nanorods array chip for DNA detection, b) fluorescence intensity comparison between free fluorescence and the one attached to Au nanorods, in quenching and enhancement modes, and c) calibration curve of detection chip with complementary single strain DNA in different concentrations. Reproduced with permission.^[7] Copyright 2017, American Chemical Society.

Photothermal harvesting devices, the most straightforward and efficient platforms, directly convert solar energy to thermal energy. Common photothermal devices (e.g., solar thermal collectors), composed of an absorber and working fluid, are mostly assembled in flat-plate forms. These collectors employ absorbers to convert sunlight to thermal energy and transport it by using a working fluid. However, the conventional design of almost all solar thermal collectors is inefficient due to the low absorption efficiency, as well as the high losses during the energy transportation. Therefore, nanofluids, supplemented with metallic NPs (e.g., plasmonic and metallic compounds, and carbon materials) dispersed in working fluid can eliminate drawbacks of these collectors by improving the absorption efficiency and providing a localized conversion of solar energy on the spot. The performance of solar thermal collectors depends on the optical absorption and concentration of particles in nanofluids.

A wide range of particles has been explored to improve the performance of photothermal harvesting devices with high absorption efficiency.^[102] Compared to other nanomaterials, plasmonic NPs stand out with extraordinary large absorption cross sections, broad and adjustable absorption spectra.^[103] Plasmonic NPs dispersed in the working fluid generate a localized heat at the surface that accelerates a direct and highly efficient solar steam generation. The improvement of solar thermal collectors has been applied as a pollution-free and inexhaustible approach, for example, in power generation and seawater deionization. **Figure 15a–c** illustrates Au-nanofluid based steam generation that gained a great energy conversion (more than 300%) compared to a solar thermal collector filled with pure water as the fluid.^[78] **Figure 15d,e** shows that the TiO₂/Ag composites efficiently enhanced the absorption of solar energy,

which helps increase the temperature of the fluid.^[103] Hybrid nanomaterials composed of photocatalytic nanomaterials (e.g., Au-TiO₂, and Au-SiO₂, etc.) have also been explored due to their high permittivity and initial absorption spectrum of plasmonic components, significantly enhanced the performance of solar energy devices.^[104] Plasmonic nanoparticles assembled into a 3D supporting template, besides the direct dispersion in working fluids, can alternatively improve solar energy absorption up to 96%, for example, by depositing Al NPs into the side-wall of the porous aluminum oxide membrane (a large number of NPs self-assembled in a closed-packed layer through the metal evaporation system). The assembly of plasmonic nanomaterials opens up the possibility of hierarchical structure design and large-scale production, providing a feasible approach for the utilization of solar energy in water desalination (e.g., portable plasmon-enhanced solar desalination device).^[105]

Photovoltaic system is one of the most representative devices for cost-effectively using solar energy to directly generate electricity. Indeed, photovoltaic effect by absorbing light generates electron-hole pairs in the junction converting solar energy to electricity. During the process, two viable ways for improving efficiency are increasing light absorption and avoiding electron-hole pair recombination; however, there is a competition between these two ways as one requires thick absorption layer, while the other one requires thin one. To tackle this problem, plasmonic NPs with their unique optical properties can be employed to improve the solar cell efficiency by using i) the large scattering cross section of particles leading to the direction change of light propagation, ii) the field enhancement at the surface of particles, and iii) carrier generation in the substrate.^[106]

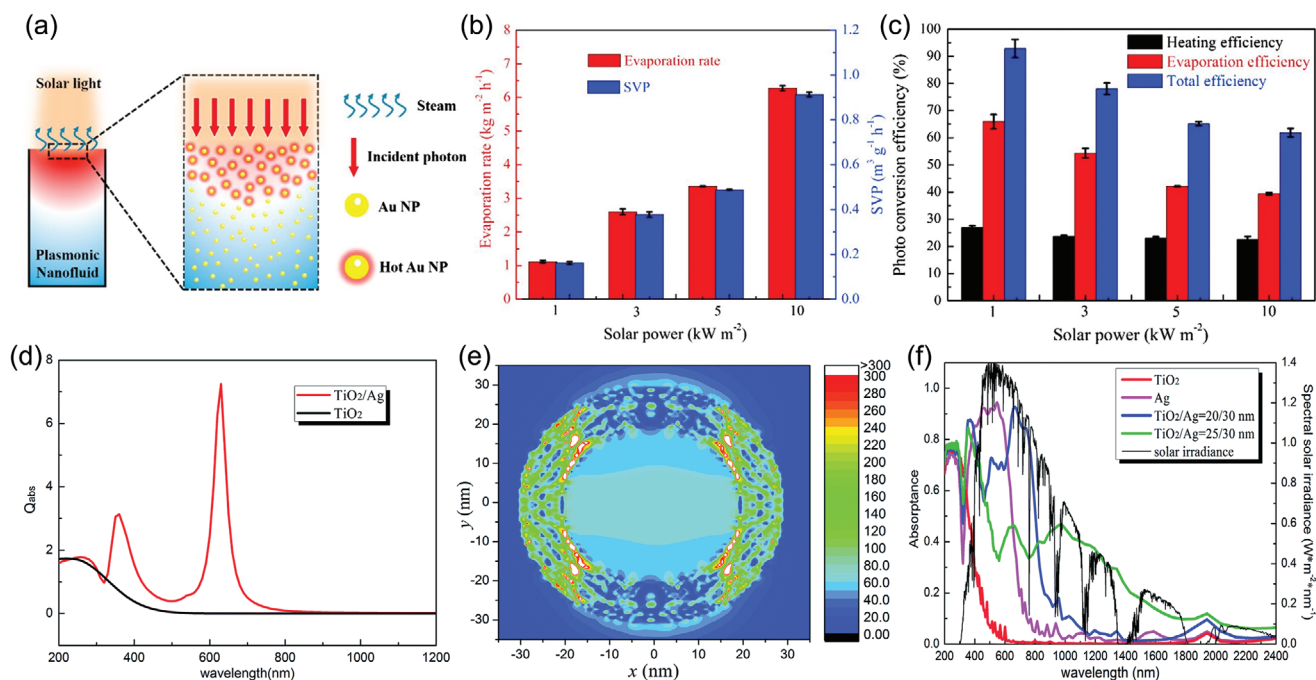


Figure 15. a) Schematic of the plasmonic nanofluid enabled direct solar steam generation. The effect of solar power intensity on b) the evaporation rate and specific vapor productivity (SVP), as well as c) heating efficiency, evaporation efficiency, and total efficiency. Reproduced with permission.^[78] Copyright 2017, Elsevier B.V. d) Absorption efficiency (Q_{abs}) of TiO_2/Ag core/shell NPs and TiO_2 NPs, e) simulation of the electric field of TiO_2/Ag core/shell NPs at the resonance peak (630 nm wavelength), and f) absorbance of different nanofluids based on TiO_2 , Ag and TiO_2/Ag core/shell NPs compared with the spectrum of solar irradiance. Reproduced with permission.^[103] Copyright 2014, Royal Society of Chemistry.

The greater light absorption can be resulted from an effective elongating light path in the semiconductor materials due to large scattering produced by the nanoparticles.^[107] Indeed, plasmonic NPs deposited on the surface of the semiconductor substrate tend to scatter light ($\approx 96\%$) into the substrate with a high refractive index rather than to the air.^[99b,108] When the scattered light reflected by the bottom side of the device, plasmonic NPs can reflect light back into the absorption layer and increase the amount and effective path of light in the absorption layer, thus improving the absorption efficiency. With the dominate scattering mechanism involved in plasmon-assisted photovoltaic devices, various metallic NPs (e.g., Au, Ag, Al, and Cu NPs) can effectively improve the performance of solar cells.

Due to the confined dimension of field enhancement and high-efficient light absorption, plasmonic NPs can be deposited into the ultrathin layer of solar cells. Cho et al. employed a layer of Ag nanostructures into an active layer of the textile polymer solar cells as a wearable device. The plasmonic nanostructures improve light absorption within this thin active layer of textile to achieve $\approx 8.71\%$ energy conversion efficiency and 20% improvement compared to the planar devices without the nanostructures.^[109] Liu et al. synthesized Au@Ag nanocuboids (for organic photovoltaics) and tuned the thickness of Ag shell to broaden the scattering spectral range of the implemented NPs. With a broad scattering effect, nanocuboids embedded in Poly(3,4-ethylenedioxythiophene)-poly(styrenesulfonate) (PEDOT:PSS) layer (Figure 16a) have improved the photovoltaic performance (up to 22.8% improvement and 10.42% average efficiencies of solar cells), whereas nanocuboids embedded into a bulk heterojunction (BHJ) active

layer (Figure 16b) have shown an inefficient performance due to the quenching, caused by the direct contact of Ag and heterojunctions. Au@Ag nanocuboids with different dimensions of Au core and Ag coating layer lead to various extinction spectra (Figure 16c). To eliminate the quenching effect, an extra silica decoration of Ag can increase the power conversion efficiency to more than 10% for the organic photovoltaics.^[7c] In fact, deposition of plasmonic NPs into the active layer of organic and perovskite solar cells is a well-known strategy in which an insulating layer (e.g., silica, titania, and other oxide semiconductor) can be used to cover the deposited plasmonic NPs and improve compatibility.^[106a] Metzman et al. also demonstrated the polystyrene (PS) functionalization plays an important role when AgNPs embedded into the active layer of organic photovoltaics (Figure 16d). Although Figure 16e shows a severe deterioration (67% power conversion efficiency decrease) by using the unfunctionalized AgNPs, the additional PS functionalization on AgNPs increased power conversion efficiency ($\approx 32\%$) compared to reference platforms without AgNPs.^[110] In most cases, dispersion of plasmonic NPs within different layers of these types of photovoltaic devices increases the light absorption and facilitates electron transportation, and improves the efficiency of photovoltaic devices.

Facing energy shortage and pollution problems, semiconductor photocatalysis converts photo energy to chemical energy similar as the photosynthesis of plants. This strategy converts solar energy by using SiO_2 , TiO_2 , and other semiconductors, and produces clean energy (e.g., H_2 , CH_4 , and CO , etc.) from water and CO_2 . Besides the energy conversion, solar light can also be used to induce organic decomposition, applicable for

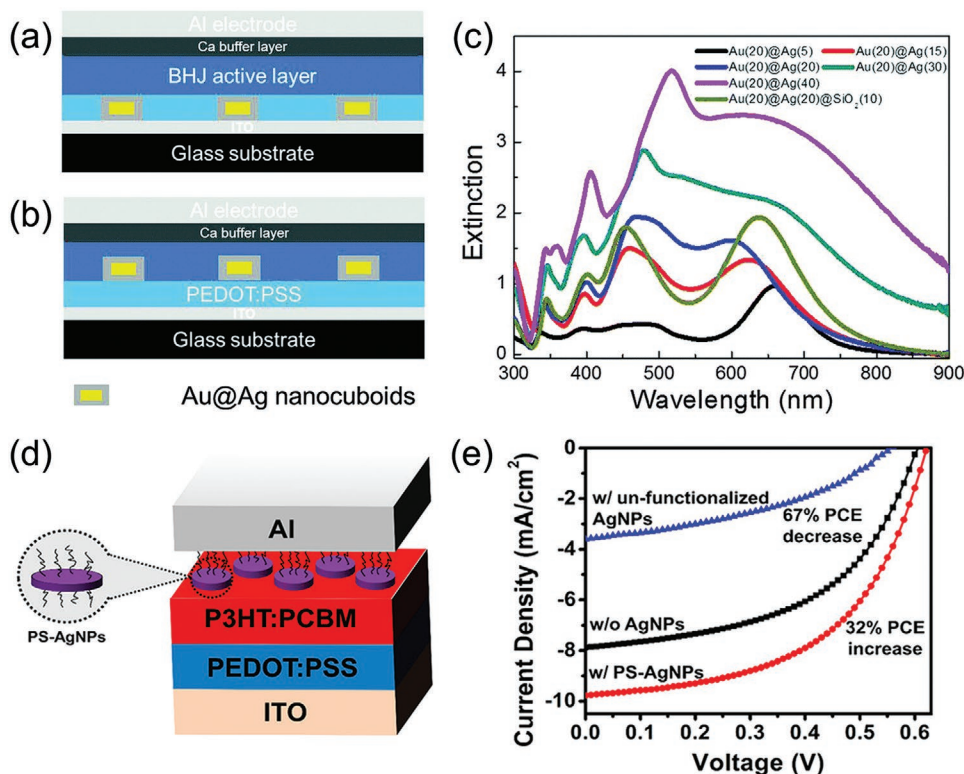


Figure 16. Schematic of Au@Ag nanocuboids embedded in a) Poly(3,4-ethylenedioxythiophene)-poly(styrenesulfonate) (PEDOT:PSS) layer, and b) bulk heterojunction (BHJ) active layer for organic photovoltaics. c) Extinction spectrum of Au@Ag nanocuboids with different Ag shell thicknesses, as indicated in the legend. Reproduced with permission.^[74] Copyright 2016, Royal Society of Chemistry. d) Schematic of organic photovoltaic device assembled by using polystyrene (PS) functionalized AgNPs. e) The current density of the organic photovoltaic device with un-functionalized and PS functionalized AgNPs compared to a reference device without nanostructures. Reproduced with permission.^[110] Copyright 2019, American Chemical Society.

eliminating pollution. However, due to the wide-band gap/large energy barrier of these semiconductors, only a small percentage of sun light ($\approx 4\%$ UV light) can be harvested for the conversion.^[111] To tackle this problem, plasmon-enhanced photocatalysis employs plasmonic NPs to increase efficiency of the oxidation reaction or reduce the energy barrier, required for the reduction reaction using visible light from the sun. The strong light-matter interaction creates resonant electrons (hot electrons) mostly similar to the mentioned processes involved in photovoltaics. These hot electrons facilitate the electron transfer not only on the surface of plasmonic NPs, but also between their interfaces with the semiconductor. For example, AuNPs can be implemented into a plasmon-enhanced photocatalysis platform to harvest methane and ethane under visible light with the surface electron transfer. Continuous-wave laser in the visible spectral range can be applied for the excitation of plasmon and the irradiated AuNP provides the hot electrons, which can activate CO₂ for the reduction. One or two electrons transferred to the absorbed CO₂ in order to be reduced to hydrocarbon products, including CH₄ and C₂H₆ (Figure 17a).^[112] Varying excitation laser wavelength to generate higher energy excitation can form heavier hydrocarbons, for example, mostly C₂H₆ in this particular case. The production rate of each NP for generating CH₄ and C₂H₆ (the turnover frequency) strongly depends on the applied excitation wavelengths (Figure 17b–d). Other plasmonic NPs, provide a broad and tunable optical resonance, can also cover the whole visible spectrum facilitating the

photocatalysis. Since semiconductors play an important role for photocatalysis, plasmonic doped TiO₂ and SiO₂ can efficiently tune the working range of the spectrum benefitted.^[111] Platinum with outstanding catalysis properties has suffered from the resonance in UV region, <300 nm. By modulating the surrounding media, Zhang et al. extended the resonance to the visible range and the absorbed light is applied to photoredox reaction by designing a 3D structure with SiO₂ core coated with small platinum NPs (2–5 nm) and a thin layer of titanium dioxide. Taking advantage of small platinum NPs with high surface-to-volume ratio, this nanostructure conserved the excellent catalysis properties suitable for the development of platinum NP-based photocatalysis.^[113]

4.3. Information Technology

Light manipulation through the modulation of plasmonic features of metallic NPs can break the diffraction limit of $\lambda/2$ in conventional optics. Overcoming the far-field diffraction limit, plasmonic NPs are able to code the information by using near-field techniques. Plasmonic-based structural color systems that create transmission filters, reflective color printing, and field-enhancement sensors are mainly based on light absorption and scattering,^[114] as well as field enhancement effects. Plasmonic NPs enable color-encoding at the nanoscale and behave as a “nanopixel,” showing advantages over the microscale dye-based

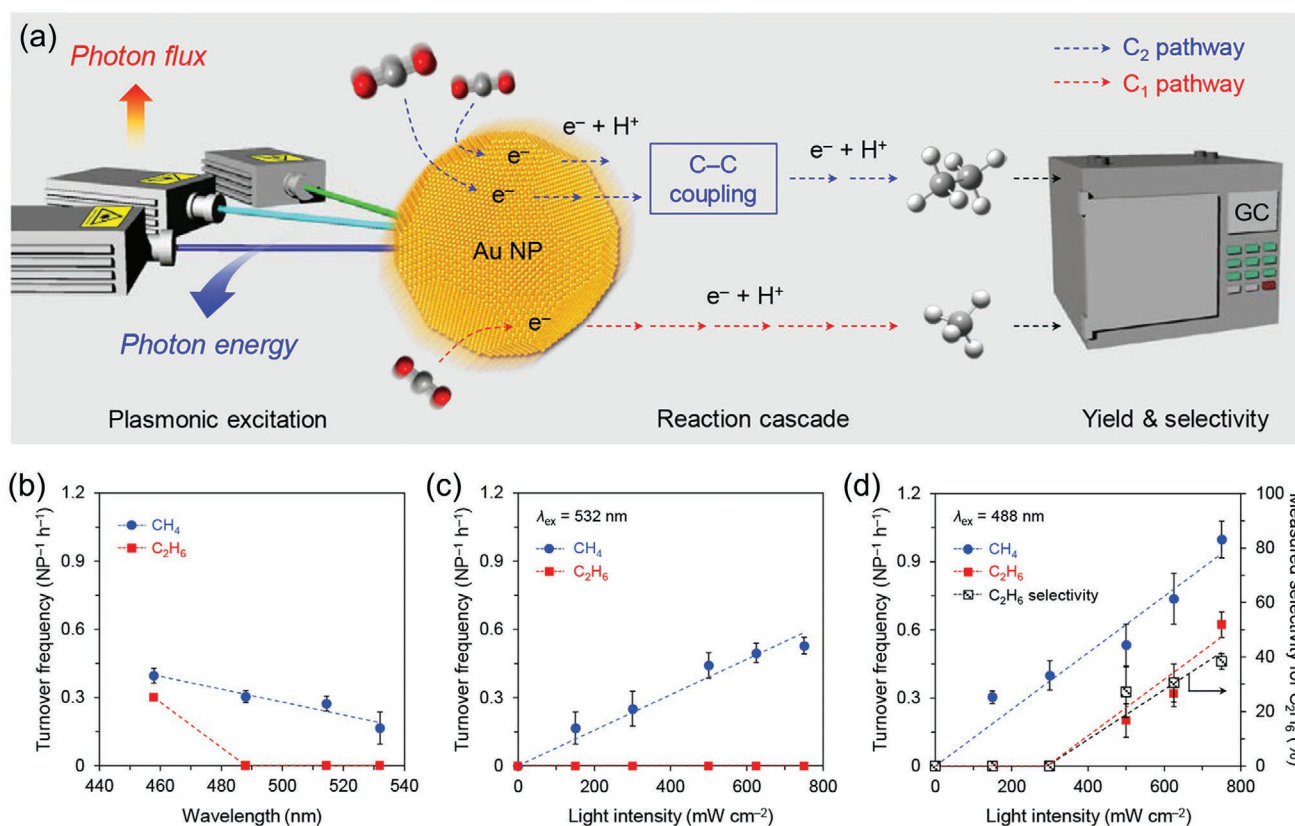


Figure 17. a) Schematic of the visible-light-driven CO₂ reduction on the surface of AuNP used to produce hydrocarbons, analyzed by gas chromatography (GC). b) Turnover frequency of CH₄ and C₂H₆ with different excitation wavelengths, and c,d) a quantitative comparison of turnover frequency of CH₄ and C₂H₆ under 532 and 488 nm excitation. Reproduced with permission.^[112] Copyright 2018, American Chemical Society.

systems in terms of resolution. Depending on the nano-formulation and the illumination condition, final display and detection can be controlled through the plasmonic properties of NPs, and the spectral range and polarization of light.

Instead of organic dyes, plasmonic filters based on noble metallic nanostructures, adjustable in morphology and distance between each other, are remarkably stable and these filters have been widely employed to separate specific discrete colors from white light due to their plasmonic absorption.^[115] Two fabrication strategies based on the plasmonic absorption mechanism have been mainly implemented by using i) an array of plasmonic NPs on substrates and ii) an array of cavity apertures.^[7h,115a,116] For example, dual-state plasmonic nanopixels (full range of standard RGB region with different polarizations of white light) have been established by creating aperture arrays on Alumina film (Figure 18a–d). The transmission information can also be doubled by changing only the light polarization, using the same full color and polarization-dependent filter under bright field microscope. For example, Figure 18b–i,b–ii shows respectively the transmission color under *x*- and *y*-polarized white light by implementing a plasmonic-based polarization dependent filter.

The information storage technique based on the scattering effect, shape- and size-dependent LSPR and polarization (similar to the mechanisms based on the light absorption mentioned above), has frequently been employed in a reflective color printing technology.^[117] The ability of gap-plasmonic alumina nanodisks has been demonstrated for a saturated and dark color

encoding.^[7h] Under varying the physical features (e.g., diameter and dimension) of nanodisks and adjusting the periodicity of nanodisks, the arrays can tune the primary color and gradually alter the color saturation. Accordingly, the color pattern “nano” with individual building blocks (Figure 18e,f) has been built, showing a wide color range. Dark color has also been obtained by combining nanodisks with different sizes in the same pixel in order to create a stronger absorption of light in the broad spectrum. In another study, Chen and Reinhard fabricated the assembled nano pixels in the visible range through a precise procedure controlling size and geometry of Au and AgNPs.^[7d] Various colors in a visible range can be designed due to the NP-dependent scattering spectrum. Accordingly, spherical and rod shape plasmonic NPs applied as “nano-pixel” in different assemblies (scanning electron microscope and scattering color images as shown in Figure 18g) have enlarged the color generation possibility due to the multi-dimension control at the nanoscale.

Due to the large absorption and scattering cross section of metallic NPs, the improved contrast can dramatically eliminate the detection limitation for writing and reading of optical information. The plasmonic nanostructures can also boost the inadequate efficiency of photodetectors through a size reduction of pixels, and meanwhile generate faster writing and reading speeds and reduce power consumption with the enhanced intensity. Furthermore, the morphology- and polarization-dependent properties of plasmonic NPs could potentially improve storage

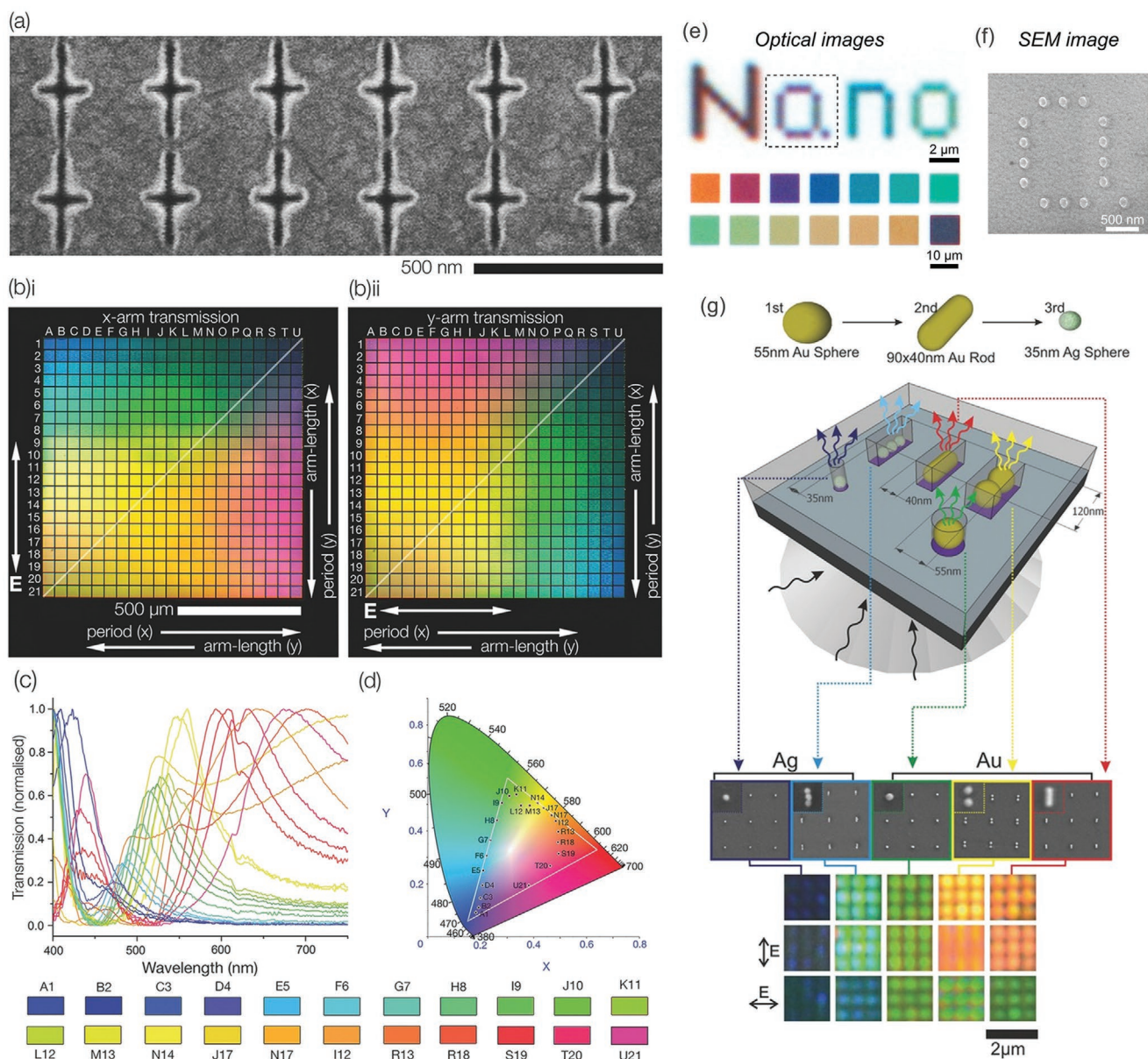


Figure 18. a) SEM images of fabricated cross-structure pixel arrays, b) transmission color of filter with varying arm-length under b-i) x and b-ii) y polarized white-light, as well as c) transmission spectra and d) CIE XY chromaticity diagram of pixel arrays labeled in (b-i). Reproduced with permission.^[115a] Copyright 2017, John Wiley & Sons, Inc. e) Optical and f) SEM image of subwavelength color printing “Nano”, with pixel in 300 nm × 300 nm square, and the various colored optical image induced by varying diameter of nanodisks. Reproduced with permission.^[7h] Copyright 2016, American Chemical Society. g) Scheme of Au nanospheres, Au nanorods, and Ag nanospheres as color pixels and their SEM and darkfield images. Reproduced with permission.^[7d] Copyright 2016, John Wiley & Sons, Inc.

density by means of composing different well-designed nanostructures and varying illumination condition in the same area.

A combination of different SERS reporters with a specific characteristic peak can be designed for information encoding.^[118] Owing to the fingerprint Raman peaks from the reporters, the encoding becomes promising for anti-counterfeiting applications. While the Raman signal is quite low, an array of plasmonic nanomaterials with the surface enhancement properties can assist to achieve high density information storage with an enough signal intensity. For example, Ag nanopillar arrays have been employed in a SERS assisted encryption through an

encoding mechanism involved fluorescent and Raman reporters to achieve an information density up to 17 000 ppi (pillar per inch).^[119] Fluorescence and SERS were simultaneously applied in the information encoding to boost the security of the encryption. In SERS-based information storage, since the characteristic peaks are sharp, and a wide range of reporters can be chosen and combined with each other easily. The design of multi SERS reporters with different characteristic Raman shift peaks can increase the encoding capacity. High versatility and efficiency can be achieved with the combination of reporters enhanced by plasmonic NPs arrays embedded in various 2D and 3D patterns.^[120]

5. Conclusions and Future Perspectives

Plasmonic NPs as a promising nanomaterial have been successfully applied in biomedical, energy, and information technology due to their unique plasmonic and optical features, including an extraordinary absorption, scattering, and field enhancement. This review focused on the fundamentals of optical properties of plasmonic NPs and discussed their interaction with light, and their other effective features (e.g., morphology, composition, and metal-permittivity) for a successful development of application-oriented nanostructures. Mie theory and numerical simulations describing the phenomena have been used as a guide to verify and optimize the designed structures and properties needed to be implemented for different applications in biomedical, energy and information technologies.

Although plasmonic NPs with tunable optical properties have been rapidly developed, the large-scale utilizations are still limited probably because of i) the relatively high price of noble metals, ii) the needed precise fabrication, post-fabrication approaches and cost effectiveness, and iii) the limited chemical stability under complexed environment and unclear biological toxicity. Due to the relative costliness and low natural abundance, recycling noble metals still requires such an improvement to avoid pollution and huge energy consumption compared to that of traditional ways (e.g., aqua regia, N-bromosuccinimide, pyridine, and mixtures of thionyl chloride).^[121] Alternatively, deep understanding of optical properties, reducing the usage of plasmonic NPs (e.g., minimizing their weight in the platforms), and combining with other types of metals (e.g., Cu and Al materials) can remarkably assist the development of cost-effective and efficient optical platforms. In most applications, the synthesis of plasmonic NPs has to be well-controlled because of strong dependency of their optical properties on the composition, size, morphology, and spatial distance between each other. Attention must therefore be paid to adapt the fabrication and post-fabrication technologies for achieving well-controlled and cost-effective application-oriented nanostructures. To stabilize plasmonic-metal NPs while conserving the optical properties, many efficient surface modification strategies have been successfully used by means of polymers and inorganic coatings, contributing to the chemical and biological stability. However, cytotoxicity and genotoxicity issues still remain a challenge for clinical practices (e.g., imaging, detection, and therapy), due to the long-term interaction between plasmonic nanostructures and intracellular compartments by triggering complexed biochemical and biological mechanisms. Therefore, the development of multifunctional plasmonic nanostructures for establishing a safe and efficient theranostic approach is a major breakthrough toward clinical translation.

Compared to other nanomaterials, optical properties of plasmonic NPs applicable in biomedical applications have superior advantages. The intrinsic permittivity of metals with an adjustable spectral range (e.g., UV, visible, and NIR) can facilitate the therapeutic features of plasmonic NPs for biomedical applications and future clinical translation. Even suffering from lower biocompatibility compared to certain kinds of nanomaterials (e.g., porous silicon, lipid, and poly(lactic-co-glycolic acid) NPs), well-established functionalization techniques have been developed for plasmonic NPs to achieve long-term dispersibility, biocompatibility, and chemical stability.^[122] A broad range

of plasmonic nanostructures has been designed for specific absorption and scattering spectra as well as “hot-spots” for field enhancement. The large adsorption cross section of plasmonic NPs and their contrast between surrounding tissue enabled the localized photothermal effect, precise hyperthermia treatment, photoacoustic imaging and optoporation phenomena, while minimizing irreversible damages to healthy cells and tissues. Ongoing human clinical developments for cancer treatment is under actual intensive study.^[53,123] The large scattering cross section generated by plasmonic NPs made them outstanding biomarkers, with tunable color and quantification properties, for bioimaging and diagnostics. The sensitivity of surrounding media of plasmonic NPs has also induced the high-sensitive biosensing. Field-enhancement effects of plasmonic nanostructured substrates with the field-enhancement effects have also been employed for boosting Raman and fluorescent signals, which enabled enormous enhancement, creating strong signal and high sensibility required to develop ultra-sensitive bioimaging and biosensing devices for clinical practices.

Plasmonic NPs are also considered to improve energy devices based on different technologies, including photothermal, photovoltaics, and photocatalysis. A wide range of absorption spectra, high scattering efficiency and “hot electron” generation improve the light absorption, energy transition efficiency and overcome the energy barrier of semiconductors in such devices with a valuable improved performance.

The plasmonic NPs have also provoked creative designs for improving information technology in storage and encryption. Tunable absorption and scattering properties of plasmonic NPs, and their formulated assemblies and arrays provide a broad range of colors and saturation displays. Higher information density has been introduced by combining a well-designed and -controlled illumination spectrum and polarization. The field-enhancement of plasmonic nanostructured substrates providing such a high level of the enhancement factor has enabled a fast and sensitive information coding and detection.

Taken together, due to their chemical and optical stability, as well as their easy fabrication and functionalization strategies, plasmonic NPs with their well-known features can address critical limitations and challenges to achieve the best performance in biomedical, energy and information technologies. Ongoing fundamental studies on plasmonics (e.g., developing practical features related to nanostructures and their properties) will open up new possibilities for designing efficient application-orientated plasmonic NPs.

Acknowledgements

This work was supported by the TransMedTech Institute Medical Technology Innovation Fund, the Canada First Research Excellence Fund, the National Science and Engineering Research Council of Canada (NSERC, funding reference number RGPIN-2018-05288 and CHRPJ-523671-18), and the Canada Institutes of Health Research (CIHR, funding reference number CPG-158264). M.H.K. was supported by a TransMedTech Institute Fellowship.

Conflict of Interest

The authors declare no conflict of interest.

Keywords

biomedical applications, energy and information technologies, Mie theory, optical properties, plasmonic-metal nanoparticles

Received: June 26, 2020

Revised: August 3, 2020

Published online:

- [1] a) U. Kreibig, M. Vollmer, *Optical Properties of Metal Clusters*, Springer Science & Business Media, Springer-Verlag, Berlin, Heidelberg **2013**; b) G. V. Hartland, *Chem. Rev.* **2011**, *111*, 3858.
- [2] E. Cottancin, N. Del Fatti, V. Halté, *Nanocoalloys: Synthesis, Structure and Properties*, Springer-Verlag, London **2012**, p. 331.
- [3] a) K. L. Kelly, E. Coronado, L. L. Zhao, G. C. Schatz, *J. Phys. Chem. B.* **2003**, *107*, 668; b) S. M. Amini, *J. Therm. Biol.* **2019**, *79*, 81; c) Y. Liu, Z. Liu, D. Huang, M. Cheng, G. Zeng, C. Lai, C. Zhang, C. Zhou, W. Wang, D. Jiang, H. Wang, B. Shao, *Coord. Chem. Rev.* **2019**, *388*, 63; d) X. Duan, S. Kamin, N. Liu, *Nat. Commun.* **2017**, *8*, 14606; e) C. Zong, M. Xu, L.-J. Xu, T. Wei, X. Ma, X.-S. Zheng, R. Hu, B. Ren, *Chem. Rev.* **2018**, *118*, 4946.
- [4] a) J. Prakash, S. H. Sun, H. C. Swart, R. K. Gupta, *Appl. Mater. Today* **2018**, *11*, 82; b) J. S. DuChene, G. Tagliabue, A. J. Welch, W. H. Cheng, H. A. Atwater, *Nano Lett.* **2018**, *18*, 2545; c) J. Shu, Z. Qiu, S. Lv, K. Zhang, D. Tang, *Anal. Chem.* **2018**, *90*, 2425.
- [5] a) L. Jauffred, A. Samadi, H. Klingberg, P. M. Bendix, L. B. Oddershede, *Chem. Rev.* **2019**, *119*, 8087; b) Z. Xi, H. Ye, X. Xia, *Chem. Mater.* **2018**, *30*, 8391.
- [6] a) S. H. Lee, B. H. Jun, *Int. J. Mol. Sci.* **2019**, *20*, 865; b) K. Kluczyk, C. David, J. Jacak, W. Jacak, *Nanomaterials* **2019**, *9*, 3; c) H. Kang, J. T. Buchman, R. S. Rodriguez, H. L. Ring, J. Y. He, K. C. Bantz, C. L. Haynes, *Chem. Rev.* **2019**, *119*, 664.
- [7] a) A. M. Wilson, J. Mazzaferri, É. Bergeron, S. Patskovsky, P. Marcoux-Valiquette, S. Costantino, P. Sapieha, M. Meunier, *Nano Lett.* **2018**, *18*, 6981; b) L. Wang, C. Darviot, J. Zapata-Farfan, S. Patskovsky, D. Trudel, M. Meunier, *J. Biophotonics* **2019**, *12*, 201900166; c) S. Liu, R. Jiang, P. You, X. Zhu, J. Wang, F. Yan, *Energy Environ. Sci.* **2016**, *9*, 898; d) T. Chen, B. M. Reinhard, *Adv. Mater.* **2016**, *28*, 3522; e) T. Köker, N. Tang, C. Tian, W. Zhang, X. Wang, R. Martel, F. Pinaud, *Nat. Commun.* **2018**, *9*, 607; f) Z. Mei, L. Tang, *Anal. Chem.* **2017**, *89*, 633; g) X. Wang, Y. He, X. Liu, L. Shi, J. Zhu, *Sol. Energy* **2017**, *157*, 35; h) M. Miyata, H. Hatada, J. Takahara, *Nano Lett.* **2016**, *16*, 3166.
- [8] a) G. V. Naik, V. M. Shalaev, A. Boltasseva, *Adv. Mater.* **2013**, *25*, 3264; b) U. Guler, V. M. Shalaev, A. Boltasseva, *Mater. Today* **2015**, *18*, 227; c) A. Comin, L. Manna, *Chem. Soc. Rev.* **2014**, *43*, 3957; d) I. Alessandri, J. R. Lombardi, *Chem. Rev.* **2016**, *116*, 14921; e) A. Agrawal, S. H. Cho, O. Zandi, S. Ghosh, R. W. Johns, D. J. Milliron, *Chem. Rev.* **2018**, *118*, 3121; f) Y. Li, Z. Li, C. Chi, H. Shan, L. Zheng, Z. Fang, *Adv. Sci.* **2017**, *4*, 1600430; g) A. Naldoni, U. Guler, Z. Wang, M. Marelli, F. Malara, X. Meng, L. V. Besteiro, A. O. Govorov, A. V. Kildishev, A. Boltasseva, V. M. Shalaev, *Adv. Opt. Mater.* **2017**, *5*, 1601031; h) M. Hasanzadeh Kafshgari, W. H. Goldmann, *Nano-Micro Lett.* **2020**, *12*, 22.
- [9] a) Y. Zhao, H. Pan, Y. Lou, X. Qiu, J. Zhu, C. Burda, *J. Am. Chem. Soc.* **2009**, *131*, 4253; b) L. Zhou, Z. Liu, Z. Guan, B. Tian, L. Wang, Y. Zhou, Y. Zhou, J. Lei, J. Zhang, Y. Liu, *Appl. Catal., B* **2020**, *263*, 118326.
- [10] a) X. Liu, X. Wang, B. Zhou, W. C. Law, A. N. Cartwright, M. T. Swihart, *Adv. Funct. Mater.* **2013**, *23*, 1256; b) D. Dorfs, T. Härtling, K. Miszta, N. C. Bigall, M. R. Kim, A. Genovese, A. Falqui, M. Povia, L. Manna, *J. Am. Chem. Soc.* **2011**, *133*, 11175; c) E. A. Hernandez-Pagan, E. H. Robinson, A. D. La Croix, J. E. Macdonald, *Chem. Mater.* **2019**, *31*, 4619.
- [11] M. Kanehara, H. Koike, T. Yoshinaga, T. Teranishi, *J. Am. Chem. Soc.* **2009**, *131*, 17736.
- [12] Q. Hao, W. Li, H. Xu, J. Wang, Y. Yin, H. Wang, L. Ma, F. Ma, X. Jiang, O. G. Schmidt, P. K. Chu, *Adv. Mater.* **2018**, *30*, 1705421.
- [13] a) M. Ono, M. Hata, M. Tsunekawa, K. Nozaki, H. Sumikura, H. Chiba, M. Notomi, *Nat. Photonics* **2020**, *14*, 37; b) K. Khaliji, S. R. Biswas, H. Hu, X. Yang, Q. Dai, S.-H. Oh, P. Avouris, T. Low, *Phys. Rev. Appl.* **2020**, *13*, 011002.
- [14] a) J. Guo, S. Li, Z. He, Y. Li, Z. Lei, Y. Liu, W. Huang, T. Gong, Q. Ai, L. Mao, Y. He, Y. Ke, S. Zhou, B. Yu, *Appl. Surf. Sci.* **2019**, *483*, 1037; b) S. A. Ghopry, M. A. Alamri, R. Goul, R. Sakidja, J. Z. Wu, *Adv. Opt. Mater.* **2019**, *7*, 1801249.
- [15] S. Chen, E. S. H. Kang, M. Shiran Chaharsoughi, V. Stanishev, P. Kühne, H. Sun, C. Wang, M. Fahlman, S. Fabiano, V. Darakchieva, M. P. Jonsson, *Nat. Nanotechnol.* **2020**, *15*, 35.
- [16] J. Olson, S. Dominguez-Medina, A. Hoggard, L.-Y. Wang, W.-S. Chang, S. Link, *Chem. Soc. Rev.* **2015**, *44*, 40.
- [17] a) P. K. Jain, X. H. Huang, I. H. El-Sayed, M. A. El-Sayed, *Acc. Chem. Res.* **2008**, *41*, 1578; b) A. Espinosa, J. Reguera, A. Curcio, Á. Muñoz-Noval, C. Kuttner, A. Van de Walle, L. M. Liz-Marzán, C. Wilhelm, *Small* **2020**, *16*, 1904960.
- [18] a) A. I. Henry, J. M. Bingham, E. Ringe, L. D. Marks, G. C. Schatz, R. P. Van Duyne, *J. Phys. Chem. C* **2011**, *115*, 9291; b) L. A. Austin, M. A. Mackey, E. C. Dreaden, M. A. El-Sayed, *Arch. Toxicol.* **2014**, *88*, 1391.
- [19] a) P. B. Johnson, R. W. Christy, *Phys. Rev. B* **1972**, *6*, 4370; b) E. D. Palik, *Handbook of Optical Constants of Solids*, Academic press, San Diego, CA **1998**.
- [20] D. Rioux, S. Vallières, S. Besner, P. Muñoz, E. Mazur, M. Meunier, *Adv. Opt. Mater.* **2014**, *2*, 176.
- [21] N. W. Ascroft, N. D. Mermin, *Solid State Physics*, Holt, Rinehart and Winston, New York **1976**.
- [22] E. A. Coronado, G. C. Schatz, *J. Chem. Phys.* **2003**, *119*, 3926.
- [23] M. B. Cortie, A. M. McDonagh, *Chem. Rev.* **2011**, *111*, 3713.
- [24] G. Mie, *Ann. Phys.* **1908**, *330*, 377.
- [25] M. Rycenga, C. M. Cobley, J. Zeng, W. Li, C. H. Moran, Q. Zhang, D. Qin, Y. Xia, *Chem. Rev.* **2011**, *111*, 3669.
- [26] a) D. Rioux, *Ph.D. Thesis*, École Polytechnique de Montréal, **2015**; b) LP2L, Numerical tools – NFMie program, <http://lp2l.polymtl.ca/en/outils> (accessed: June 2020).
- [27] a) W. Zhang, P. Gu, Z. Wang, B. Ai, Z. Zhou, Z. Zhao, C. Li, Z. Shi, G. Zhang, *Adv. Opt. Mater.* **2019**, *7*, 1901337; b) H. K. Lee, Y. H. Lee, Q. Zhang, I. Y. Phang, J. M. R. Tan, Y. Cui, X. Y. Ling, *ACS Appl. Mater. Interfaces* **2013**, *5*, 11409.
- [28] a) Q. Zhang, N. Large, P. Nordlander, H. Wang, *J. Phys. Chem. Lett.* **2014**, *5*, 370; b) J. Reguera, J. Langer, D. J. de Aberasturi, L. M. Liz-Marzán, *Chem. Soc. Rev.* **2017**, *46*, 3866; c) H. H. Jeong, A. G. Mark, M. Alarcon-Corraea, I. Kim, P. Oswald, T. C. Lee, P. Fischer, *Nat. Commun.* **2016**, *7*, 1.
- [29] a) A. Bansal, S. Verma, *J. Opt.* **2016**, *45*, 7; b) E. R. Encina, E. A. Coronado, *J. Phys. Chem. C* **2016**, *120*, 5630; c) C. Loo, A. Lin, L. Hirsch, M.-H. Lee, J. Barton, N. Halas, J. West, R. Drezek, *Technol. Cancer Res. Treat.* **2004**, *3*, 33.
- [30] a) X. Huang, S. Neretina, M. A. El-Sayed, *Adv. Mater.* **2009**, *21*, 4880; b) H. J. Chen, L. Shao, Q. Li, J. F. Wang, *Chem. Soc. Rev.* **2013**, *42*, 2679.
- [31] R. v. Gans, *Ann. Phys.* **1915**, *352*, 270.
- [32] a) M. Yorulmaz, S. Nizzero, A. Hoggard, L.-Y. Wang, Y.-Y. Cai, M.-N. Su, W.-S. Chang, S. Link, *Nano Lett.* **2015**, *15*, 3041; b) J. He, C. He, C. Zheng, Q. Wang, J. Ye, *Nanoscale* **2019**, *11*, 17444.
- [33] J. Zhao, A. O. Pinchuk, J. M. McMahon, S. Li, L. K. Ausman, A. L. Atkinson, G. C. Schatz, *Acc. Chem. Res.* **2008**, *41*, 1710.
- [34] M. Hu, J. Chen, Z.-Y. Li, L. Au, G. V. Hartland, X. Li, M. Marquez, Y. Xia, *Chem. Soc. Rev.* **2006**, *35*, 1084.
- [35] J. P. Kottmann, O. J. F. Martin, R. S. David, S. Sheldon, *New J. Phys.* **2000**, *2*, 27.

- [36] E. J. Zeman, G. C. Schatz, *J. Phys. Chem.* **1987**, *91*, 634.
- [37] S. Kim, J. M. Kim, J. E. Park, J. M. Nam, *Adv. Mater.* **2018**, *30*, 1704528.
- [38] a) U. Aslam, S. Linic, *Chem. Mater.* **2016**, *28*, 8289; b) L. Huang, J. Zou, J.-Y. Ye, Z.-Y. Zhou, Z. Lin, X. Kang, P. K. Jain, S. Chen, *Angew. Chem.* **2019**, *131*, 8886.
- [39] a) D. Rioux, M. Meunier, *J. Phys. Chem. C* **2015**, *119*, 13160; b) D. Rioux, M. Meunier, *Google Patents US10239122B2*, **2016**.
- [40] S. Patskovsky, E. Bergeron, D. Rioux, M. Simard, M. Meunier, *Analyst* **2014**, *139*, 5247.
- [41] M. A. García, *J. Phys. D: Appl. Phys.* **2011**, *44*, 283001.
- [42] E. Prodan, P. Nordlander, N. Halas, *Chem. Phys. Lett.* **2003**, *368*, 94.
- [43] a) R. Bardhan, S. Mukherjee, N. A. Mirin, S. D. Levit, P. Nordlander, N. J. Halas, *J. Phys. Chem. C* **2010**, *114*, 7378; b) J. Zhu, J. J. Li, J. W. Zhao, *Plasmonics* **2013**, *8*, 417; c) J. A. I. Acapulco, S. Hong, S. K. Kim, S. Park, *J. Colloid Interface Sci.* **2016**, *461*, 376.
- [44] a) I. Pastoriza-Santos, C. Kinnear, J. Pérez-Juste, P. Mulvaney, L. M. Liz-Marzán, *Nat. Rev. Mater.* **2018**, *3*, 375; b) E. Bergeron, C. Boutopoulos, R. Martel, A. Torres, C. Rodríguez, J. Niskanen, J.-J. Lebrun, F. M. Winnik, P. Sapieha, M. Meunier, *Nanoscale* **2015**, *7*, 17836.
- [45] a) E. Chaffin, R. T. O'Connor, J. Barr, X. Huang, Y. Wang, *J. Chem. Phys.* **2016**, *145*, 054706; b) S. Schlücker, *Angew. Chem., Int. Ed.* **2014**, *53*, 4756; c) K. Kim, Y. M. Lee, J. W. Lee, K. S. Shin, *Langmuir* **2009**, *25*, 2641.
- [46] a) A. Bucharskaya, G. Maslyakova, G. Terentyuk, A. Yakunin, Y. Avetisyan, O. Bibikova, E. Tuchina, B. Khlebtsov, N. Khlebtsov, V. Tuchin, *Int. J. Mol. Sci.* **2016**, *17*, 1295; b) D. Yang, G. Yang, P. Yang, R. Lv, S. Gai, C. Li, F. He, J. Lin, *Adv. Funct. Mater.* **2017**, *27*, 1700371.
- [47] Z. Qin, J. C. Bischof, *Chem. Soc. Rev.* **2012**, *41*, 1191.
- [48] C. Darvot, P. Hardy, M. Meunier, *J. Biophotonics* **2019**, *12*, 201900193.
- [49] a) P. Yuan, X. Ding, Y. Y. Yang, Q.-H. Xu, *Adv. Healthcare Mater.* **2018**, *7*, 1701392; b) D. Wang, S. C. Pillai, S.-H. Ho, J. Zeng, Y. Li, D. D. Dionysiou, *Appl. Catal., B* **2018**, *237*, 721; c) P. C. Ray, S. A. Khan, A. K. Singh, D. Senapati, Z. Fan, *Chem. Soc. Rev.* **2012**, *41*, 3193.
- [50] a) M.-F. Tsai, S.-H. G. Chang, F.-Y. Cheng, V. Shanmugam, Y.-S. Cheng, C.-H. Su, C.-S. Yeh, *ACS Nano* **2013**, *7*, 5330; b) T. Yata, Y. Takahashi, M. M. Tan, H. Nakatsuji, S. Ohtsuki, T. Murakami, H. Imahori, Y. Umeki, T. Shiomi, Y. Takakura, M. Nishikawa, *Biomaterials* **2017**, *146*, 136; c) J. Beik, Z. Abed, F. S. Ghoreishi, S. Hosseini-Nami, S. Mehrzadi, A. Shakeri-Zadeh, S. K. Kamrava, *J. Controlled Release* **2016**, *235*, 205.
- [51] X. Huang, I. H. El-Sayed, W. Qian, M. A. El-Sayed, *J. Am. Chem. Soc.* **2006**, *128*, 2115.
- [52] a) S. M. Fothergill, C. Joyce, F. Xie, *Nanoscale* **2018**, *10*, 20914; b) J.-E. Park, M. Kim, J.-H. Hwang, J.-M. Nam, *Small Methods* **2017**, *1*, 1600032; c) C. Song, F. Li, X. Guo, W. Chen, C. Dong, J. Zhang, J. Zhang, L. Wang, *J. Mater. Chem. B* **2019**, *7*, 2001.
- [53] A. R. Rastinehad, H. Anastos, E. Wajswol, J. S. Winoker, J. P. Sfakianos, S. K. Doppalapudi, M. R. Carrick, C. J. Knauer, B. Taouli, S. C. Lewis, A. K. Tewari, J. A. Schwartz, S. E. Canfield, A. K. George, J. L. West, N. J. Halas, *Proc. Natl. Acad. Sci. USA* **2019**, *116*, 18590
- [54] a) H. Sun, J. Su, Q. Meng, Q. Yin, L. Chen, W. Gu, Z. Zhang, H. Yu, P. Zhang, S. Wang, Y. Li, *Adv. Funct. Mater.* **2017**, *27*, 1604300; b) L. Luo, H. He, C. Li, Y. He, Z. Hao, S. Wang, Q. Zhao, Z. Liu, D. Gao, *ACS Biomater. Sci. Eng.* **2019**, *5*, 1321; c) Y. Li, J. Jin, D. Wang, J. Lv, K. Hou, Y. Liu, C. Chen, Z. Tang, *Nano Res.* **2018**, *11*, 3294.
- [55] a) R. Cheheltani, R. M. Ezzibdeh, P. Chhour, K. Pulaparthi, J. Kim, M. Jurcova, J. C. Hsu, C. Blundell, H. I. Litt, V. A. Ferrari, H. R. Allcock, C. M. Sehgal, D. P. Cormode, *Biomaterials* **2016**, *102*, 87; b) Z. Yang, J. Song, Y. Dai, J. Chen, F. Wang, L. Lin, Y. Liu, F. Zhang, G. Yu, Z. Zhou, W. Fan, W. Huang, Q. Fan, X. Chen, *Theranostics* **2017**, *7*, 2177; c) X. Ge, B. Chen, T. Liu, L. Wei, L. Tong, Q. Ma, S. Gao, J. Song, *RSC Adv.* **2019**, *9*, 13494.
- [56] M. Xu, L. V. Wang, *Rev. Sci. Instrum.* **2006**, *77*, 041101.
- [57] P. K. Upputuri, C. Yang, S. Huang, K. Wang, M. Wang, M. Pramanik, *J. Biomed. Opt.* **2018**, *24*, 1.
- [58] A. Hatef, B. Darvish, A. Dagallier, Y. R. Davletshin, W. Johnston, J. C. Kumaradas, D. Rioux, M. Meunier, *J. Phys. Chem. C* **2015**, *119*, 24075.
- [59] M. R. Jones, K. D. Osberg, R. J. Macfarlane, M. R. Langille, C. A. Mirkin, *Chem. Rev.* **2011**, *111*, 3736.
- [60] W. Li, X. Chen, *Nanomedicine* **2015**, *10*, 299.
- [61] L. Nie, S. Wang, X. Wang, P. Rong, Y. Ma, G. Liu, P. Huang, G. Lu, X. Chen, *Small* **2014**, *10*, 1585.
- [62] a) A. Chekkoury, J. Gateau, W. Driessen, P. Symvoulidis, N. Bézière, A. Feuchtinger, A. Walch, V. Ntziachristos, *Biomed. Opt. Express* **2015**, *6*, 3134; b) L. Cavigli, S. Centi, C. Borri, P. Tortoli, I. Panettieri, I. Streit, D. Ciofini, G. Magni, F. Rossi, S. Siano, F. Ratto, R. Pini, *J. Biophotonics* **2019**, *12*, 201900082.
- [63] J. Baumgart, L. Humbert, É. Boulais, R. Lachaine, J.-J. Lebrun, M. Meunier, *Biomaterials* **2012**, *33*, 2345.
- [64] T. K. Kim, J. H. Eberwine, *Anal. Bioanal. Chem.* **2010**, *397*, 3173.
- [65] C. Boutopoulos, E. Bergeron, M. Meunier, *J. Biophotonics* **2016**, *9*, 26.
- [66] E. Boulais, R. Lachaine, A. Hatef, M. Meunier, *J. Photochem. Photobiol., C* **2013**, *17*, 26.
- [67] a) M. Schomaker, D. Heinemann, S. Kalies, S. Willenbrock, S. Wagner, I. Nolte, T. Ripken, H. M. Escobar, H. Meyer, A. Heisterkamp, *J. Nanobiotechnol.* **2015**, *13*, 10; b) R. Lachaine, É. Boulais, D. Rioux, C. Boutopoulos, M. Meunier, *ACS Photonics* **2016**, *3*, 2158.
- [68] a) Y. Umabayashi, Y. Miyamoto, M. Wakita, A. Kobayashi, T. Nishisaka, *J. Biochem.* **2003**, *134*, 219; b) C. M. Pitsillides, E. K. Joe, X. Wei, R. R. Anderson, C. P. Lin, *Biophys. J.* **2003**, *84*, 4023.
- [69] D. Heinemann, M. Schomaker, S. Kalies, M. Schieck, R. Carlson, H. M. Escobar, T. Ripken, H. Meyer, A. Heisterkamp, *PLoS One* **2013**, *8*, 58604.
- [70] R. Lachaine, C. Boutopoulos, P.-Y. Lajoie, É. Boulais, M. Meunier, *Nano Lett.* **2016**, *16*, 3187.
- [71] a) Y. Feng, G. Wang, Y. Chang, Y. Cheng, B. Sun, L. Wang, C. Chen, H. Zhang, *Nano Lett.* **2019**, *19*, 4478; b) E. S. Melby, S. E. Lohse, J. E. Park, A. M. Vartanian, R. A. Putans, H. B. Abbott, R. J. Hamers, C. J. Murphy, J. A. Pedersen, *ACS Nano* **2017**, *11*, 5489.
- [72] K. A. Willets, A. J. Wilson, V. Sundaresan, P. B. Joshi, *Chem. Rev.* **2017**, *117*, 7538.
- [73] a) S. Patskovsky, E. Bergeron, M. Meunier, *J. Biophotonics* **2015**, *8*, 162; b) S. Patskovsky, E. Bergeron, D. Rioux, M. Meunier, *J. Biophotonics* **2015**, *8*, 401.
- [74] É. Bergeron, S. Patskovsky, D. Rioux, M. Meunier, *Nanoscale* **2016**, *8*, 13263.
- [75] K. Seekell, M. Crow, A. Chilkoti, A. Wax, S. Marinakos, J. Ostrander, *J. Biomed. Opt.* **2011**, *16*, 116003.
- [76] H. Xu, Q. Li, L. Wang, Y. He, J. Shi, B. Tang, C. Fan, *Chem. Soc. Rev.* **2014**, *43*, 2650.
- [77] a) M. Imai, K. Mine, H. Tomonari, J. Uchiyama, S. Matuzaki, Y. Niko, S. Hadano, S. Watanabe, *Anal. Chem.* **2019**, *91*, 12352; b) N. Khlebtsov, V. Bogatyrev, L. Dykman, B. Khlebtsov, S. Staroverov, A. Shirokov, L. Matora, V. Khanadeev, T. Pylaev, N. Tsyganova, G. Terentyuk, *Theranostics* **2013**, *3*, 167; c) S. E. Ochmann, C. Vietz, K. Trofymchuk, G. P. Acuna, B. Lalkens, P. Tinnefeld, *Anal. Chem.* **2017**, *89*, 13000.
- [78] A. R. Halpern, J. B. Wood, Y. Wang, R. M. Corn, *ACS Nano* **2014**, *8*, 1022.
- [79] a) X. Liu, Y. Wang, P. Chen, A. McCadden, A. Palaniappan, J. Zhang, B. Liedberg, *ACS Sens.* **2016**, *1*, 1416; b) Z. Gao, H. Ye,

- D. Tang, J. Tao, S. Habibi, A. Minerick, D. Tang, X. Xia, *Nano Lett.* **2017**, *17*, 5572; c) A. Nsamela Matombi, M. Hasanzadeh Kafshgari, L. Wang, S. Patskovsky, D. Trudel, M. Meunier, *ACS Appl. Nano Mater.* **2020**, *3*, 4171.
- [80] H. B. Jeon, P. V. Tsalu, J. W. Ha, *Sci. Rep.* **2019**, *9*, 13635.
- [81] C. Zhang, D. Paria, S. Semancik, I. Barman, *Small* **2019**, *15*, 1901165.
- [82] P. Chen, N. T. Tran, X. Wen, Q. Xiong, B. Liedberg, *ACS Sens.* **2017**, *2*, 235.
- [83] P. Chen, B. Liedberg, *Anal. Chem.* **2014**, *86*, 7399.
- [84] M. Fleischmann, P. J. Hendra, A. J. McQuillan, *Chem. Phys. Lett.* **1974**, *26*, 163.
- [85] a) S. Nie, S. R. Emory, *Science* **1997**, *275*, 1102; b) C. Zong, R. Premasiri, H. N. Lin, Y. M. Huang, C. Zhang, C. Yang, B. Ren, L. D. Ziegler, J. X. Cheng, *Nat. Commun.* **2019**, *571*, E10.
- [86] M. Rycenga, M. H. Kim, P. H. Camargo, C. Cobley, Z.-Y. Li, Y. Xia, *J. Phys. Chem. A* **2009**, *113*, 3932.
- [87] a) J.-H. Lee, J.-W. Oh, S. H. Nam, Y. S. Cha, G.-H. Kim, W.-K. Rhim, N. H. Kim, J. Kim, S. W. Han, Y. D. Suh, J.-M. Nam, *Small* **2016**, *12*, 4726; b) J. M. McLellan, Z.-Y. Li, A. R. Siekkinen, Y. Xia, *Nano Lett.* **2007**, *7*, 1013; c) B. Kuestner, M. Gellner, M. Schuetz, F. Schoeppler, A. Marx, P. Stroebel, P. Adam, C. Schmuck, S. Schluecker, *Angew. Chem., Int. Ed.* **2009**, *48*, 1950; d) N. Pazos-Perez, J. M. Fitzgerald, V. Giannini, L. Guerrini, R. A. Alvarez-Puebla, *Nanoscale Adv.* **2019**, *1*, 122.
- [88] J. Liu, J. Guo, G. Meng, D. Fan, *Chem. Mater.* **2018**, *30*, 5256.
- [89] a) Z. Fusco, R. Bo, Y. Wang, N. Motta, H. Chen, A. Tricoli, *J. Mater. Chem. C* **2019**, *7*, 6308; b) B. G. M. Vieira, N. S. Mueller, E. B. Barros, S. Reich, *J. Phys. Chem. C* **2019**, *123*, 17951.
- [90] H. Dies, A. Bottomley, D. L. Nicholls, K. Stamplecoskie, C. Escobedo, A. Docoslis, *Nanomaterials* **2020**, *10*, 661.
- [91] a) R. Schreiber, J. Do, E.-M. Roller, T. Zhang, V. J. Schüller, P. C. Nickels, J. Feldmann, T. Liedl, *Nat. Nanotechnol.* **2014**, *9*, 74; b) G. Chen, K. J. Gibson, D. Liu, H. C. Rees, J.-H. Lee, W. Xia, R. Lin, H. L. Xin, O. Gang, Y. Weizmann, *Nat. Mater.* **2019**, *18*, 169.
- [92] M. Wang, J. Dong, C. Zhou, H. Xie, W. Ni, S. Wang, H. Jin, Q. Wang, *ACS Nano* **2019**, *13*, 13702.
- [93] V. V. Thacker, L. O. Herrmann, D. O. Sigle, T. Zhang, T. Liedl, J. J. Baumberg, U. F. Keyser, *Nat. Commun.* **2014**, *5*, 3448.
- [94] a) M. D. Baaske, M. R. Foreman, F. Vollmer, *Nat. Nanotechnol.* **2014**, *9*, 933; b) H.-N. Wang, J. K. Register, A. M. Fales, N. Gandra, E. H. Cho, A. Boico, G. M. Palmer, B. Klitzman, T. Vo-Dinh, *Nano Res.* **2018**, *11*, 4005.
- [95] U. S. Dinish, G. Balasundaram, Y.-T. Chang, M. Olivo, *Sci. Rep.* **2015**, *4*, 4075.
- [96] K. Wang, S. Li, M. Petersen, S. Wang, X. Lu, *Nanomaterials* **2018**, *8*, 762.
- [97] a) M. Bauch, K. Toma, M. Toma, Q. Zhang, J. Dostalek, *Plasmonics* **2014**, *9*, 781; b) S.-H. Guo, S.-J. Tsai, H.-C. Kan, D.-H. Tsai, M. R. Zachariah, R. J. Phaneuf, *Adv. Mater.* **2008**, *20*, 1424.
- [98] J.-W. Liaw, J.-H. Chen, C.-S. Chen, M.-K. Kuo, *Opt. Express* **2009**, *17*, 13532.
- [99] J.-F. Li, C.-Y. Li, R. F. Aroca, *Chem. Soc. Rev.* **2017**, *46*, 3962.
- [100] S. Tu, D. Rioux, J. Perreault, D. Brouard, M. Meunier, *J. Phys. Chem. C* **2017**, *121*, 8944.
- [101] a) H. A. Atwater, A. Polman, *Nat. Mater.* **2010**, *9*, 205; b) S. Pillai, M. A. Green, *Sol. Energy Mater. Sol. Cells* **2010**, *94*, 1481; c) S. Linic, P. Christopher, D. B. Ingram, *Nat. Mater.* **2011**, *10*, 911; d) M. J. Kale, T. Avanesian, P. Christopher, *ACS Catal.* **2014**, *4*, 116; e) A. Furube, S. Hashimoto, *NPG Asia Mater* **2017**, *9*, 454; f) L. Zhou, S. Zhuang, C. He, Y. Tan, Z. Wang, J. Zhu, *Nano Energy* **2017**, *32*, 195.
- [102] H. Ren, M. Tang, B. Guan, K. Wang, J. Yang, F. Wang, M. Wang, J. Shan, Z. Chen, D. Wei, H. Peng, Z. Liu, *Adv. Mater.* **2017**, *29*, 1702590.
- [103] Y. Xuan, H. Duan, Q. Li, *RSC Adv.* **2014**, *4*, 16206.
- [104] a) L. Yi, S. Ci, S. Luo, P. Shao, Y. Hou, Z. Wen, *Nano Energy* **2017**, *41*, 600; b) H. Duan, L. Tang, Y. Zheng, C. Xu, *Appl. Therm. Eng.* **2018**, *133*, 188.
- [105] L. Zhou, Y. Tan, J. Wang, W. Xu, Y. Yuan, W. Cai, S. Zhu, J. Zhu, *Nat. Photonics* **2016**, *10*, 393.
- [106] a) K. Yao, H. J. Zhong, Z. L. Liu, M. Xiong, S. F. Leng, J. Zhang, Y. X. Xu, W. Y. Wang, L. Zhou, H. T. Huang, A. K. Y. Jen, *ACS Nano* **2019**, *13*, 5397; b) X. Chen, M. Gu, *ACS Appl. Energy Mater.* **2019**, *2*, 2094.
- [107] a) S. H. Jeong, H. Choi, J. Y. Kim, T. W. Lee, *Part. Part. Syst. Charact.* **2015**, *32*, 164; b) S. W. Baek, G. Park, J. Noh, C. Cho, C. H. Lee, M. K. Seo, H. Song, J. Y. Lee, *ACS Nano* **2014**, *8*, 3302.
- [108] K. R. Catchpole, A. Polman, *Opt. Express* **2008**, *16*, 21793.
- [109] S. H. Cho, J. Lee, M. J. Lee, H. J. Kim, S.-M. Lee, K. C. Choi, *ACS Appl. Mater. Interfaces* **2019**, *11*, 20864.
- [110] J. S. Metzman, A. U. Khan, B. A. Magill, G. A. Khodaparast, J. R. Heflin, G. Liu, *ACS Appl. Energy Mater.* **2019**, *2*, 2475.
- [111] a) V. Kumaravel, S. Mathew, J. Bartlett, S. C. Pillai, *Appl. Catal., B* **2019**, *244*, 1021; b) C. P. Li, P. Wang, H. J. Li, M. M. Wang, J. Zhang, G. H. Qi, Y. D. Jin, *Nanoscale* **2018**, *10*, 14290.
- [112] S. Yu, A. J. Wilson, J. Heo, P. K. Jain, *Nano Lett.* **2018**, *18*, 2189.
- [113] N. Zhang, C. Han, Y.-J. Xu, J. J. Foley Iv, D. Zhang, J. Codrington, S. K. Gray, Y. Sun, *Nat. Photonics* **2016**, *10*, 473.
- [114] S. J. Tan, L. Zhang, D. Zhu, X. M. Goh, Y. M. Wang, K. Kumar, C.-W. Qiu, J. K. W. Yang, *Nano Lett.* **2014**, *14*, 4023.
- [115] a) E. Heydari, J. R. Sperling, S. L. Neale, A. W. Clark, *Adv. Funct. Mater.* **2017**, *27*, 1701866; b) C. S. H. Hwang, M. S. Ahn, Y. Lee, T. Chung, K. H. Jeong, *Sci. Rep.* **2019**, *9*, 9082.
- [116] A. Gentile, F. Ruffino, M. Grimaldi, *Nanomaterials* **2016**, *6*, 110.
- [117] a) Y. Gu, L. Zhang, J. K. W. Yang, S. P. Yeo, C.-W. Qiu, *Nanoscale* **2015**, *7*, 6409; b) J. Feng, F. Yang, X. Wang, F. Lyu, Z. Li, Y. Yin, *Adv. Mater.* **2019**, *31*, 1900789.
- [118] Z. Wang, S. Zong, L. Wu, D. Zhu, Y. Cui, *Chem. Rev.* **2017**, *117*, 7910.
- [119] Y. Liu, Y. H. Lee, Q. Zhang, Y. Cui, X. Y. Ling, *J. Mater. Chem. C* **2016**, *4*, 4312.
- [120] Y. Liu, Y. H. Lee, M. R. Lee, Y. Yang, X. Y. Ling, *ACS Photonics* **2017**, *4*, 2529.
- [121] a) W. Lin, R.-W. Zhang, S.-S. Jang, C.-P. Wong, J.-I. Hong, *Angew. Chem., Int. Ed.* **2010**, *49*, 7929; b) C. Yue, H. Sun, W.-J. Liu, B. Guan, X. Deng, X. Zhang, P. Yang, *Angew. Chem., Int. Ed.* **2017**, *56*, 9331; c) J.-L. Do, D. Tan, T. Friščić, *Angew. Chem., Int. Ed.* **2018**, *57*, 2667.
- [122] a) M. H. Kafshgari, N. H. Voelcker, F. J. Harding, *Nanomedicine* **2015**, *10*, 2553; b) P. Yingchoncharoen, D. S. Kalinowski, D. R. Richardson, *Pharmacol. Rev.* **2016**, *68*, 701; c) J. Ghitman, E. I. Biru, R. Stan, H. Iovu, *Mater. Des.* **2020**, *193*, 108805.
- [123] M. R. K. Ali, Y. Wu, M. A. El-Sayed, *J. Phys. Chem. C* **2019**, *123*, 15375.



Lu Wang received her B.Ing. and M.Ing. degrees in Materials Science and Engineering from Donghua University in 2014 and 2016, respectively. She is currently a Ph.D. candidate in the department of Engineering Physics at the Polytechnique Montréal. She joined the Laser Processing and Plasmonics Laboratory (LP²L) in 2016. Her research focuses on plasmonic nanostructures design, and biomedical imaging and biosensing applications.



Morteza Hasanzadeh Kafshgari is a TransMedTech Research Associate in the department of Engineering Physics at the Polytechnique Montréal, Canada. He received his Ph.D. degree in Materials Science from the University of South Australia in 2016, and then joined the University of Erlangen-Nuremberg, Germany, as an Alexander von Humboldt postdoctoral fellow. His interdisciplinary research is focused on the development and application of new biomaterials and technologies in nanomedicine.



Michel Meunier received his B.Ing. and M.Sc.A. degrees in Engineering Physics from Polytechnique Montréal in 1978 and 1980, respectively, and his Ph.D. degree from the Massachusetts Institute of Technology in 1984. He is the director of the department of Engineering Physics at the Polytechnique Montréal, and a fellow of the SPIE, OSA and the Canadian Academy of Engineering. He also held in 2002–2016 a Canadian Research Chair in laser micro/nanoengineering of materials. His research is focused on fundamental and biomedical applications of plasmonic nanostructures and laser processing of various materials.